ADSORPTION OF HCN AND H_2S OVER ZnO AND Al-DOPED ZnO MONOLAYER: FIRST PRINCIPLES STUDY

A Dissertation

Submitted to the Department of Physics, Amrit Campus
Tribhuvan University in the Partial Fulfillment for the Requirement
of Master's Degree of Science in Physics

By

Dipak Oli

Exam Roll No.: 3564/PHY-076

January 4, 2024

RECOMMENDATION

This is to certify that **Mr. Dipak Oli** has successfully completed the dissertation entitled " **ADSORPTION OF HCN AND H_2S OVER ZnO AND Al-DOPED ZnO MONOLAYER: FIRST PRINCIPLES STUDY"** under my supervision and guidance.

I recommend this work as a completed one in order to partially fulfill the requirement for the Master's Degree of Science in Physics, at Tribhuvan University.

Parajuli

.....

Supervisor

Prof. Dr. Rajendra Parajuli

Amrit Campus, Tribhuvan University

Thamel Kathmandu

ACKNOWLEDGEMENTS

I would like to express my sincere gratitude to Prof. Dr. Rajendra Parajuli, Department of Physics, Amrit Science Campus for his unwavering support, instruction, guidance, and motivation during my work, as a supervisor.

I gratefully express my deep appreciation to Prof. Dr. Leela Pradhan Joshi (Immediate past Head of Department), Asst. Prof. Pitamber Shrestha (Coordinator of the MSc. Program), Dr.Hari Krishna Neupane, and other professors, for guiding me to enlighten my Knowledge.

Similarly, I would also like to acknowledge the International Science Program (ISP) for providing us with computer and VASP software during our research work. And, I am grateful to Prof. Dr. Shriram Sharma for coordinating with ISP and that helped us receive this precious opportunity.

Last but not least, I sincerely thank my family members, friends, and relatives for their constant support, motivation, and encouragement in research activities.

EVALUATION

This is to certify that the Dissertation entitled " **ADSORPTION OF HCN AND H_2S OVER ZnO AND Al-DOPED ZnO MONOLAYER: FIRST PRINCIPLES STUDY"** submitted by **Mr.Dipak Oli** is very good and we reached in conclusion that the work partially fulfills the requirement of Master's Degree of Physics.

Evaluation Committee

.....

Prof. Dr. Rajendra Parajuli

Supervisor

Department of Physics

Amrit Campus, Kathmandu

.....

Associate Prof. Dr. Janak Ratna Malla

Head of Department Department of Physics Amrit Campus, Kathmandu

.....

Asst. Prof. Pitamber Shrestha

Coordinator, Department of Physics

Amrit Campus, Tribhuvan University

Thamel Kathmandu

.....

External Examiner

.....

Internal Examiner

Date: ..D.e.c. 11, 2023

ABSTRACT

The adsorption of HCN and H_2S molecules in 3× 3× 1 monolayer and Al- doped ZnO, replacing one Zn-atom by Al-atom was studied in spin-polarized DFT by applying the Vienna Ab initio Simulation Package (VASP). Various exchange-correlation functionals like GGA-PBE, meta GGA-SCAN, and DFT+U using a basis set namely PAW (Projected Augmented Wave) pseudopotential were employed in order to determine the structural, electronic, and magnetic properties of the pristine and Al- doped ZnO before and after the adsorption of HCN and H_2S. ZnO monolayer and the ZnO adsorbed with HCN and H_2S were found to be non-magnetic whereas Al-doped ZnO upon the adsorption of HCN and H_2S was found to be magnetic in nature. Similarly, the lattice parameters of ZnO were found to be increasing with the presence of foreign elements. The outcome thus achieved is nearly identical and in good agreement with the earlier theoretical investigations.

सार

प्रस्तुत शोध प्रबन्धमा हामीले भास्प (VASP) सफ्टवेयरको प्रयोग गरी शुद्ध जिङ्क अक्साइड र आलुमिनियम डप गरेको जिङ्क अक्साइडलाई हाइड्रोजन सलफाइड (H_2S) र हाइड्रोजन साइनाइडले (HCN) सोख्नु पूर्व र सोखिसकेपछि उक्त यौगिकको संरचनात्मक गुण, चुम्बकिय गुण र इलेक्ट्रोनिक गुणहरूको अध्ययन गरेका छौं। उक्त कार्य सम्पन्न गर्नका निम्ति GGA-PBE, Meta GGA-SCAN र DFT+U फङ्सनलको प्रयोग गरका छौं। यसो गर्दा हामीले ZnO मोनोलिएर, Al-ZnO, HCN-ZnO, H_2S-ZnO मा चुम्बकिय गुण नभएको पायौं तथा Al-HCN-ZnO र Al-H_2S-ZnO मा भने थोरै मात्रामा चुम्बकिय गुण भएको पायौं। त्यस्तै उक्त यौगिकमा बाह्य तत्वको समावेश गर्दा ल्याटिस प्यारामिटरहरू बढ्दै गएको पायौं। यसरी प्राप्त भएका नतिजाहरू अघिल्ला अनुसन्धानसँग लगभग समान रहेका छन्।

List of Figures

List of Tables

List of Abbreviations

Al	Aluminium
DFT	Density Functional Theory
DOS	Density of State
eV	electron Volt
GGA	Generalized Gradient Approximation
HF	Hartree-fock
H_2S	Hydrogen Sulfide
HCN	Hydrogen cyanide
LDA	Local Density Approximation
mGGA	meta-Generalized Gradient Approximation
PAW	Projected Augmented Wave
PBE	Perdew-Burke-Ernzerhof
PDOS	Projected Density Of States
SCF	Self Consistent Field
TDOS	Total Density Of States
VASP	Vienna Ab initio Simulation Package
VBM	Valence Band Maximum
VESTA	Visualisation for Electronic Structural Analysis
XC	Exchange Correlaton
ZnO	Zinc Oxide

Contents

Chapter 1

Introduction

1.1 General Consideration

Exploring strongly correlated systems like Zinc Oxide [1] by using various software like Vienna Ab initio Simulation Package (VASP) [2] is gaining huge prominence among young researchers day by day. Until 2003, it was believed that two-dimensional (2D) materials did not exist; whereby it was thought that these 2D materials might easily transform into a three-dimensional (3D) state if existed. The situation now is quite different; more than 700 2D crystal structures have been proven to be theoretically stable, and only a small number of these have been synthesized to this point. The study of nano-sheets greatly advanced after the discovery of 2D graphene in 1994 [3].
Since the discovery of graphene, two-dimensional (2D) materials have received much study attention. Their distinct optical, electrical, gas sensing and mechanical features have the potential to be used as essential elements in cutting-edge optoelectronic and electronic applications [4]. These fundamental and application-related interests have drawn researchers to use theoretical and experimental methods to get an understanding of the origins of these phenomena, including crystal structure, electrical, surface, and optical properties, as well as how they respond to external fields [5].

1.2 Zinc Oxide

At ambient temperature, ZnO is an n-type transparent semiconductor with a broadband gap of almost 3.4 eV and a high binding energy of 60 meV [6]. It can be found in three

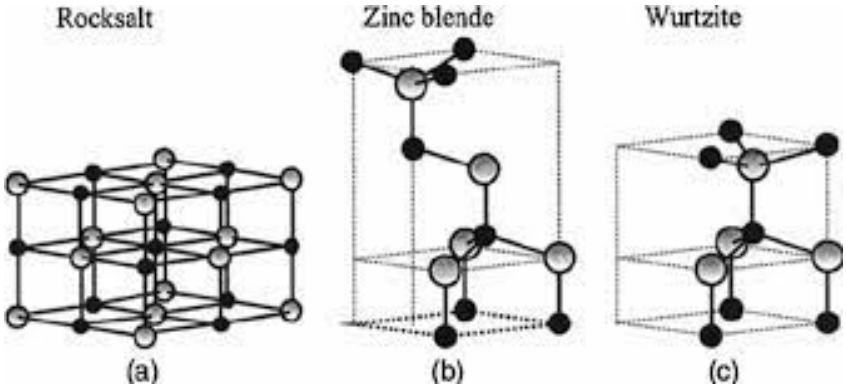

Figure 1.1: Crystal structure of ZnO : (a) rock salt (B1), (b) cubic zinc-blende(B3) and (c) hexagonal wurtzite (B4) [1]

forms: hexagonal wurtzite structure, cubic rock salt, and cubic zinc-blende. Among them, the most stable is hexagonal wurtzite whereas others are unstable. The only way to stabilize the zinc blend is to grow it on a cubic substrate with rock salt. Under relatively high pressure, they are stable [1]. The crystal structure of different forms of ZnO is shown in Figure 1.1. The concentration of free electrons, the concentration of foreign atoms, external strain, and temperature are the key factors affecting the lattice parameter of semiconductors. For hexagonal ZnO, the lattice parameter a is found in the range of 0.5204 to 0.5207nm whereas the c/a ratio varies from 0.1593 to 0.1603. Moreover, ZnO lies in the II-VI group [7].

With its particular characteristics of a broad and direct band gap, high electron mobility, and potent piezoelectric and pyroelectric reactions, zinc oxide (ZnO) is a practical and intensively researched semiconductor material. These characteristics make ZnO an excellent choice for LEDs, solar cells, sensors, transistors, and other devices.

1.2.1 Electronic Properties

One of the aspects of ZnO that has been investigated the most, is its electronic characteristics. Mostly, the density of states (DOS) and energy band structure are computed to reflect the electronic behavior of ZnO, which is helpful in device design. A semiconductor's band structure plays a significant role in determining how useful it might be, the knowledge of which is very helpful in predicting the family of materials for device applications. In the case of ZnO, the difference between the upper valence band and lower conduction band lies at the same place in the Brillouin zone, i.e. K=0, which

proves that ZnO has a direct band gap of ≈ 3.4 eV [6, 8]

1.2.2 Magnetic properties

Generally, the hexagonal structure of ZnO is non-magnetic in nature, because of its paired electron spins produced by the arrangement of its atoms. However, weak magnetism can be produced by adding certain materials or causing flaws. Isolated unpaired electrons result from flaws in the crystal structure, such as oxygen or zinc vacancies, and they help to produce magnetism [9]. Additionally, the partially filled electron shells of some elements when introduced can produce magnetic behavior. As a result of side effects, this is most obvious at the nanoscale. The magnetic characteristics of ZnO are generally weak [10].

1.2.3 Doping

Doping is the deliberate insertion of impurities into a compound in order to modify its structural, magnetic, electrical, and optical properties [11, 12]. Doping is a strategic method in material engineering that turns ordinary materials into highly effective substances with specialized features, spurring innovation in a variety of technical domains. Doping can be characterized into two types: n-type and p-type doping. If we introduce the elements having extra electrons then it is considered n-type doping otherwise p-type doping [13].

1.2.3.1 Aluminium

A silver-white, non-magnetic metal, aluminum is prized for its excellent lightweight, resistance to corrosion, and low density. Since it interacts easily with oxygen and other elements, it forms an oxide layer on its surface to shield it from further corrosion. Aluminum is incredibly resistant to rust [14] and degradation because of the formation of the natural oxide layer. Due to its unique features, Aluminium is used in a wide variety of fields like transportation, construction, food packaging, and many more. In our work, we doped our system (ZnO) with an Aluminium atom in place of Zn-atom.

1.2.4 Adsorption

Adsorption is the technique of capturing molecules of gas, liquids, or solute in the form of a thin layer. Such an accumulation in the material drastically alters the system's magnetic, optical, electrical, mechanical, thermal, and piezoelectric capabilities [15]. To locate and categorize different gases, electronic equipment known as gas sensors are utilized, which are widely used to detect explosives or dangerous gases and measure gas concentrations. Furthermore, gas sensors are utilized in manufacturing and industrial settings to detect gas leakage. Basically, Adsorption can be classified into two types. They are:

- **Physical Adsorption**

  In physical adsorption or physisorption, molecules or atoms are attracted to a solid or liquid surface by relatively weak forces of attraction known as adsorbents. Van der Waals forces, London dispersion forces, and interactions between dipoles are some of these forces. Physisorption normally takes place at low temperatures and moderate pressures, and it is reversible. Applications for physisorption include the adsorption of gases in activated carbon and the adsorption of water vapor, among others.

- **Chemical Adsorption**

  The adsorbate and the adsorbent interact chemically more strongly during chemical adsorption or chemisorption. During chemisorption, chemical bonds are made or destroyed, which causes the adsorbate to cling to the surface. This kind of adsorption is typically selective and it frequently causes both the adsorbate and the adsorbent to undergo irreversible modifications. For instance, the adsorption of H_2 gas in the metal surface is known as chemical adsorption.

For our research work, we computed the adsorption energy by using the following formula:

$$E_{ads} = E_{ZnO} - E_{HCN}$$

$$E_{ads} = E_{ZnO} - E_{H_2S}$$

$$E_{ads} = E_{Al-ZnO-HCN} - E_{Al-ZnO} - E_{ZnO} - E_{HCN}$$

$$E_{ads} = E_{Al-ZnO-H_2S} - E_{Al-ZnO} - E_{ZnO} - E_{H_2S}$$

where,

E_{ZnO} = Total energy of ZnO

E_{Al-ZnO} = Total energy of AL-doped ZnO

E_{HCN} = Energy of isolated HCN

E_{H_2S} = Energy of isolated H_2S

$E_{Al-ZnO-H_2S}$ = Total energy of H_2S adsorbed Al-doped ZnO

$E_{Al-ZnO-HCN}$ = Total energy of HCN adsorbed Al-doped ZnO

If the energy thus calculated is positive then this implies that the interaction is strong and stable i.e. exothermic whereas negative energy represents weaker interactions i.e. endothermic.

1.2.4.1 Hydrogen Sulfide

Hydrogen sulfide is a colorless, toxic gas that smells like rotten eggs and is heavier than air. H_2S is frequently used in a variety of manufacturing processes, including those for coal, oil, gasoline, sewage, and natural gas. Meanwhile, if the normal permitted limit is surpassed, this colorless, combustible, and highly poisonous gas might have a detrimental impact on human health that causes headaches, irritability, dizziness, and many more. According to a survey, it is revealed that if the human body is exposed to H_2S gas at levels of 250 ppm and higher, it may result in neurobehavioral damage or even death [16, 17]. Therefore, it is crucial to track such a dangerous gas for monitoring and control purposes.

1.2.4.2 Hydrogen Cynaide

Hydrogen cyanide, HCN is a highly toxic compound, which consists of hydrogen, carbon, and nitrogen. It is colorless and smells faintly of almonds. Extremely dangerous HCN interferes with cellular respiration, resulting in the impairment of the body's ability to use oxygen. Even a small amount of HCN can be lethal due to its extreme toxicity. Going through its positive aspects, it is manufactured synthetically for a variety of industrial uses, including the creation of plastics, dyes, and pesticides, as well as naturally in some plants.

1.3 Literature Review

The electrical, elastic, structural, and optical properties of wurtzite ZnO were investigated by M. Yaakob, N. Hussin, et al. using the CASTEP code and density functional theory with LDA and DFT + U technique. They discovered that the elastic characteristics and lattice parameters were closer to the value found in normal experiments. Their research shows that DFT+U greatly enhances both the elastic and electrical characteristics. Additionally, DFT+U provides a better description of the localization of Zn 3d electrons, a transition metal [18].

On the basis of DFT and using CASTEP software, C. Tan, D. Sun, and their research team examined the phase stability, electrical, and optical properties of Mn-doped ZnO for the very first time. They imply DFT+U ($U_{d,Zn}$ = 10 eV, $U_{p,O}$ = 7eV) in 4 x 4 monolayer and obtain a band gap of 3.36 eV for bulk, 4.01 eV to 6.21 eV on rising the concentration of Mg from 0.0625 to 0.75. They discovered that the system's band gap widens as the Mg content increases. When the Mg concentration is greater than 75 percent, they also noticed a change in the MgZnO monolayer's direct-to-indirect band gap. Moreover, they discovered that Mg doping causes the optical absorption peak to shift to blue [19].

H.C Wu, Y.C Peng et al. studied the structural, electronic, and optical properties of Ga-doped ZnO (one Zn atom is replaced by Ga atom) on varying the concentration of Ga using the first principle by employing Hubbard U (DFT + U_d+ U_p) functional in CASTEP code. The band gap and lattice constants thus computed, are comparable to earlier experimental results. Additionally, they came to the conclusion that synthesis of Ga-doped ZnO becomes challenging at high doping concentrations due to the need for higher formation energy. However, as the concentration of Ga increases, the optical band gap and donor concentration also increase. This helps to raise the conductivity and transmittance. Similarly, electrical conductivity is decreased by 25 percent due to localized states that are close to the Fermi level and an increased possibility of free electron scattering. They also mentioned that selecting an appropriate concentration of the doping material obviously leads to fruitful results [20].

The electronic, structural, and optical characteristics of Al-doped ZnO were investigated by M. Wu, D. Sun, C. Tan, and their research team, using density functional theory and the CASTEP algorithm. To arrive at their conclusion, they assume that DFT+U (U_d, Zn = 10 eV, U_p, O = 7eV) functional in 4 x 4 monolayer and 2 x 2 x 2 supercell of bulk wurtzite ZnO. They discovered that the Al-doped ZnO exhibits the maximum visibility in almost all circumstances as compared to the bulk system as they continuously increased the concentration of Al. Additionally, at 12.5 percent Al concentration, vision is at its greatest. They discovered that due to quantum confinement effects, the band gap of both pure and Al-doped ZnO is larger than that of bulk systems. Due to the donor state being close to the fermi level, when Al is doped in the system, the fermi level is displaced to the conduction band. They proposed that the promising transparent electrode for nanoscale optoelectronic devices is an Al-doped ZnO monolayer [21].

D.R Lawati, R. Parajuli, and their research team studied the structural, electronic, mechanical, and optical characteristics of $MgZnO_3$ perovskite by using the First principles under VASP code. They employed PBE, PBEsol SCAN, DFT+U (U= 4eV), and HSE06 exchange-correlation functional to explore the aforementioned properties of the $MgZnO_3$. They discovered that the cubic phase of the perovskite is structurally, chemically, and mechanically stable. Similarly, through precise analysis of the mechanical properties of $MgZnO_3$, they discovered that the material is crystalline, stable, rigid, ductile, and has a metal-ionic bond. Additionally, they found that perovskite has indirect band gap energy, and the material is highly recommended for optoelectronic devices due to its sound optical features [22].

B. Qiao, P. Zhao, and their research team studied the adsorption of NO gas in ZnO monolayer and Al-doped ZnO monolayer ($4 \times 4 \times 1$) by applying the First principles under the CASTEP code. They explored that the minimal physical adsorption was used by the NO molecule to interact with ZnO; however, the NO molecule was capable of adhering chemically to Al-doped ZnO. They also found that there is a huge magnification in the adsorption energy of NO in Al-doped ZnO as compared to pristine ZnO. Their research showed that the Al-doped ZnO monolayer is an outstanding material to adsorb NO gas, which gets improvised due to external electric fields [23].

Q. Wang and his research team investigated the adsorption behavior of CO in ZnO mono-layer ($5 \times 5 \times 1$) using DFT under the VASP code. They employed the GGA-PBE exchange-correlational functional in order to explore the structural and electronic stability as well as the catalytic activity of Al-doped ZnO. Upon replacing one Zn atom with an Al atom, electrons get shifted in the conduction band, which improves the conductance as well as the chemical activity of the system. They concluded that CO gas sensing is outstanding for Al-doped ZnO at low temperatures. Moreover, through this research, they introduced important details about how Al-doped ZnO nanostructures detect reducing gases like CO and ethanol [24].

S. Rezaie et.al studied the carbon-doped ZnO nanotube-based hydrogen gas sensor theoretically. They had replaced the oxygen atom in order to dope the carbon atoms in the ZnO. They explore the sensor response to hydrogen gas using the first-principles density functional theory by employing PBE functional using the SIESTA package. After computing the adsorption energy, they concluded that the hydrogen gas is chemically adsorbed to the carbon atom strongly [25].

Z. Pan and his research group used the DMol package with PBE functional to study the adsorption behavior of CO and HCHO over Cu-doped ZnO. They discovered that the Cu dopant likes to be trapped on the T_O site of the ZnO surface with the binding energy (E_b) of around 1.08 eV, and the n-doping for Cu-decorating on the ZnO surface could be extrapolated, leading to the zero bandgap for the Cu-ZnO system. Additionally, two systems with E_{ad} of 2.04 and 1.66 eV, respectively, had chemisorption detected, and the gas adsorptions had no effect on the Cu-ZnO monolayer's metallic characteristic. The energy gap widens from the Cu-ZnO system's 1.32 eV to the CO and HCHO systems' 1.68 and 1.72 eV, respectively, indicating a discernible change in the electrical conductivity of the Cu-ZnO monolayer in the ambient CO and HCHO [26].

1.4 Objectives

The general objective of our research work is to study the adsorption behavior of hydrogen sulfide (H_2S) and hydrogen cyanide (HCN) in pristine mono-layer and Al-doped zinc oxide.

The specific objectives of the research work are:

- To study the electronic and magnetic properties of pristine ZnO mono-layer and Al-doped ZnO.
- To study the electronic and magnetic properties of ZnO, when H_2S and HCN are adsorbed in monolayer.
- To study the magnetic and electronic properties of H_2S and HCN adsorbed Al-doped ZnO.

1.5 Motivation

Due to rapid industrialization and urbanization, severe air pollution that is mostly caused by manufacturing and automotive emissions, has seen to be a serious hazard to human existence and development. Even the loss of life and property damage could be caused by the leakage of explosive and combustible gases. Therefore, the demand for real-time and efficient detection of these dangerous chemicals utilizing gas sensors is currently a need of an hour. Semiconducting metal oxide-based gas sensors have been the subject of extensive research across the globe due to their high gas responsiveness, great selectivity, outstanding mobility, and low manufacturing cost, and upon reading various national and international papers on ZnO, we learned about its wide applications in the field of gas sensing, solar cells, electronics, piezoelectric, biocompatibility, biodegradability as well as ceramics industry devices, which provided me a strong motivation to work in this system. ZnO is a novel family of two-dimensional materials with special qualities that have mostly not been investigated in the graphene-like ZnO monolayer sheet. Moreover, after reading the aforementioned publication, upon realizing that no one has used HCN and H_2S in Al-doped ZnO. We were more than inspired to do this work.

Chapter 2

Theoretical Background

2.1 General Consideration

This chapter will review the core ideas needed to perform computations in our project. We start by looking at the Schrödinger equations corresponding to the Hamiltonian formulation of many body systems. We presented a number of approximations, each with a distinct set of constraints, to solve Schrödinger equations of many body systems. These include the Born Oppenheimer (BO) approximation, which ignores nucleus motion in favor of electronic motion due to the latter's greater mass, and then the Hartee's Self-Consistent Field Approximation, followed by the Hartee-Fock Approximation. Finally, we discussed briefly Thomas Fermi (TF) and Density Functional Theory (DFT), highlighting DFT's contribution to Kohn-Sham (KS) equations by going beyond theory HF's bounds.DFT calculations are first-principles-based and do not take into account any experimental data.

2.1.1 Many Body Hamiltonian

In the theoretical study of condensed matter physics, determining the electronic structure of atoms, molecules, and bulk materials is the primary goal. Nuclei and electrons make up atoms. The electron is regarded as a wave function rather than a classical particle in quantum physics. Any time-independent quantum system's electrical structure can be solved using the Schrodinger equation. The Schrodinger equation for many body

Hamiltonian is given as

$$\hat{H}\psi = E\psi \tag{2.1}$$

where, the Hamiltonian, H can be expressed as [6]

$$\hat{H} = -\sum_{i=1}^{N}\frac{\hbar^2}{2m_e}\nabla_i^2 - \sum_{I=1}^{M}\frac{\hbar^2}{2m_I}\nabla_I^2 - \sum_{i=1}^{N}\sum_{I=1}^{M}\frac{Z_I e^2}{|r_i - R_I|} + \sum_{j>i}^{N}\sum_{i=1}^{N}\frac{e^2}{|r_i - r_j|} + \sum_{J>I}^{M}\sum_{I=1}^{M}\frac{Z_I Z_J e^2}{|R_I - R_J|} \tag{2.2}$$

where indices i, j refer to electrons; I, J refer to nuclei; m_e is the mass of the electron, and M_I and Z_I are the masses and atomic numbers of the nuclei respectively. The first and second expressions in equation 2.2 represents the kinetic energy of electrons and nuclei respectively. The remaining expression signifies the energies of electron-nucleus, electron-electron, and nucleus-nucleus coulomb interactions, respectively.

It is hard to obtain the exact solution of the many-body Schrodinger equation 2.1 so, various approximations were restored to get approximate values. Some of the approaches which are introduced to solve equation 2.1 are discussed below:

2.1.2 Born-Oppenheimer Approximation

Max Born and J. Robert Oppenheimer introduced the Born Oppenheimer (BO) approximation in 1927 [27]. It is regarded as one of the earliest, most straightforward, and widely used approaches to solving the Many Body Schrodinger problem. The entire atomic system is divided into two subsystems i.e. electronic and nuclei.

$$\psi_{total} = \psi_{electronic} \;\; X \;\; \psi_{nuclei}$$

In this approximation, nuclei remain at rest due to their heavy mass. So, we only consider the mobility of the electrons. In comparison to the velocity of nuclei, the velocity of the electron is extremely high (more than 1000 times). Therefore, it is possible to ignore the nuclei's kinetic energy [28]. Thus, the Born Approximation reduces the whole Hamiltonian as:

$$\hat{H} = -\sum_{i=1}^{N}\frac{\hbar^2}{2m_e}\nabla_i^2 - \sum_{i=1}^{N}\sum_{I=1}^{M}\frac{Z_I e^2}{|r_i - R_I|} + \sum_{j>i}^{N}\sum_{i=1}^{N}\frac{e^2}{|r_i - r_j|} \tag{2.3}$$

Then, the total energy of the electronic system is given as:

$$\begin{aligned}\hat{E}_{tot} &= \hat{H}_{tot} \\ &= T_N + V_{ee}(r) + V_{ext}\end{aligned} \tag{2.4}$$

where,

V_{ext} = electron- nuclei interaction

Variables cannot be separated because of coupled electronic coordinates in the equation 2.3. Hence, it is impossible to provide an exact solution. To solve the Schrödinger equation, we employed Hartree's self-consistent field approximation.

2.1.3 Hartree's Self-Consistent Field Approximation

This approximation assumes that the atomic system having N electrons moves independently in the combined central field produced by the nucleus and remaining (N-1) electrons. Also, the motion of each electron is described by a one-particle Schrödinger equation. Using Hartree's central field approximation, the Schrödinger wave equation for the N electrons atomic system is given by:

$$\hat{H}\psi_H(r_1, r_2, ..., r_N) = E_H\psi_H(r_1, r_2, ...r_N) \tag{2.5}$$

The minimization of total energy is:

$$\begin{aligned}E =& \langle\psi_H|\hat{H}|\psi_H\rangle \\ &= \langle\psi| - \frac{1}{2}\nabla_i^2 + \frac{1}{2}\sum_{i\neq j}^{N}\frac{1}{|r_i - r_j|} - \sum_{i}^{N}\sum_{I}^{M}\frac{Z_I}{|r_i - R_I|}|\psi\rangle\end{aligned} \tag{2.6}$$

Upon normalizing the above condition by normalizing factor:

$$\int \psi^*\psi d^3r = 1 \tag{2.7}$$

we get,

$$\left(-\frac{1}{2}\nabla_i^2 + V_{ext} + V_{SC}\right)\phi_i(r_i) = \lambda_i\phi_i(r_i) \tag{2.8}$$

where,

$$V_{ext} = \sum_i\sum_I\frac{Z_I}{|r_i - R_I|} \tag{2.9}$$

and

$$V_{SC} = \sum_{i \neq j} \int d\tau_j \frac{\left|\phi_j(r_j)\right|^2}{\left|r_i - r_j\right|} \tag{2.10}$$

The equation 2.8 is known as the Hartee equation which is computed on the basis of self-consistent. Hartee equation remains invalid as it ignores the motion of electrons due to the anti-symmetry nature. That's why, it gives the same energy for the ortho and para-state of helium atom.

2.1.4 Hartree-Fock Approximation

This approximation deals with the defect of the Hartee method and considers the spin direction of electrons. It approximates the anti-symmetric wave function in Slater determinant form as [29]:

$$\psi = \frac{1}{\sqrt{N!}} \begin{vmatrix} \phi_1(r_1, s_1) & \phi_2(r_1, s_1) & \ldots & \ldots & \phi_1(r_1, s_1) \\ \phi_1(r_2, s_2) & \phi_2(r_2, s_2) & \ldots & \ldots & \phi_1(r_2, s_2) \\ \ldots & \ldots & \ldots & \ldots & \ldots. \\ \ldots & \ldots & \ldots & \ldots & \ldots. \\ \phi_1(r_N, s_N) & \phi_2(r_N, s_N) & \ldots & \ldots & \phi_1(r_N, s_N) \end{vmatrix} \tag{2.11}$$

where,

$\frac{1}{\sqrt{N!}}$= Normalizing factor

$\phi_i = i^{th}$ single electron spin-orbital

r_i = position coordinate of i^{th} electron

s_i = spin coordinate of i^{th} electron

On solving equation 2.11, we obtained N coupled equation as:

$$\begin{aligned} \left[-\frac{1}{2}\nabla_r^2 - \sum_{i=1}^{N}\sum_{I=1}^{M}\frac{Z_I}{r_i - R_I} + \sum_{i \neq j}^{N} \int dr' \phi_j^*(r') \frac{1}{\left|r - r'\right|} \phi_j(r')\right] \phi_i(r) \\ - \sum_{i \neq j} \left[\int dr' \phi_j^*(r') \frac{1}{\left|r - r'\right|} \phi_i(r') s_i s_j\right] \phi_j(r) = \epsilon_i \phi_i(r) \end{aligned} \tag{2.12}$$

The coulomb potential/integral (J), the last component of the LHS, is a result of the interaction of interpenetrating charge distributions, which is a completely quantum phenomenon that arises from the anti-symmetric nature of the wave function for fermions.

The Hartee-Fock technique ignores the instantaneous interaction of the electrons and treats the interaction of one electron with another electron according to the mean field approximation. Given that electrons repel one another, it follows that one electron's position will have an impact on another electron's position. Additionally, if a molecule has one electron on one side, the other electron is probably on the other side. A Hartee-Fock computation does not take this effect into account. Correlation effects of this nature can be resolved via DFT, MP2, MP4, CCSD, and many more. However, we employed DFT for this work.

2.2 Density Functional Theory

The disadvantage of the Hartree-Fock technique was addressed by the development of density functional theory (DFT). In HF theory, only electrons with parallel spins are taken into account. Contrarily, the correlation caused by electron interactions with parallel and anti-parallel spins is taken into account by DFT. In fact, correlation energy is given by [30]:

$$E_{corr} = E_o - E_{HF}$$

where, E_o is the exact ground state energy and E_{HF} is ground state energy calculated by the HF method using BO approximation, in a non-relativistic approach.

DFT is more than simply another method for solving the Schrödinger equation. DFT is not only a way of parameterizing empirical data, it is also a radically distinct, theoretically rigorous technique for solving any interacting problem by mapping it perfectly to a much simpler non-interacting problem [31]. Its approach is used in a wide range of areas to solve a wide range of issues, with the ground-state electronic structure problem being the most prevalent. DFT, has lately emerged as a promising technique to solve the material modeling challenge in the field of physics, chemistry, material science, and engineering.

2.2.1 Thomas-Fermi Model

Modern density functional theory is simplified in the Thomas-Fermi (TF) model. A well-known Thomas-Fermi equation based on a statistical model is as follows:

$$\frac{5}{3}\frac{3}{10}\left(3\pi^2\right)^{\frac{2}{3}}\left(\rho(r)\right)^{\frac{2}{3}} + V_{ext}(r) + \int \frac{\rho(r')}{\left|r - r'\right|}dr' = \mu \tag{2.13}$$

where μ is the known as Lagrangian multiplier or chemical potential.
Since it excludes the actual shell structure of atoms or molecule binding, this TF model is fairly simplistic for more complex systems. It was also debatable, although fundamentally sound for DFT. The Hohenberg and Kohn theorems laid the theoretical groundwork for contemporary density functional theory after 37 years of TF theory.

2.2.2 Hohenberg-Kohn Theorems

With the publication of an important study by Hohenberg and Kohn in the Physical Review in 1964, density functional theory as we know it today, was born. The fundamental theoretical pillars upon which all contemporary density functional theories are built are the theorems proved in this article. The precision, dependability, and viability of using electron density n(r) rather than complex wavefunction were established after these theorems were published in 1964 [32]. The overall Hamiltonian can be expressed as:

$$\hat{H}_{tot} = T + V_{ee} + V_{ext} \tag{2.14}$$

where,

$$V_{ext} = \sum_{i}^{N}\sum_{I}^{M}\frac{Z_I}{\left|r_i - R_I\right|} = \sum_{i=1}^{N} V_{ext}(r_i) \tag{2.15}$$

where,
$V_{ext} = \sum_{I}^{M}\frac{Z_I}{\left|r_i - R_I\right|}$; is a system dependent external potential caused by M^{th} electron in the system's i^{th} electron.

2.2.2.1 First Hohenberg-Kohn Theorem

According to this theorem, the ground state density n(r) of a bound system of interacting electrons in an external potential $V_{ext}(r)$ is the only factor that can be used to identify

its potential $v(r)$.

If ψ_1 and H_1 be the ground state wavefunction and the Hamiltonian of the system has potential $v_1(r)$ then ground state energy E_1 can be expressed as:

$$\begin{aligned} E_1 &= \langle \psi_1 | \hat{H}_1 | \psi_1 \rangle \\ &= \int v_1(r) n(r) dr + \langle \psi_1 | (\hat{T} + \hat{V}_{ee}) | \psi_1 \rangle \end{aligned} \tag{2.16}$$

Similarly, Another potential gives other hamiltonian H_2 with wavefunction ψ_2, then

$$E_2 = \int v_2(r) n(r) dr + \langle \psi_2 | (\hat{T} + \hat{V}_{ee}) | \psi_2 \rangle \tag{2.17}$$

Since, ψ_2 is not the ground state of the $\hat{H}_1$ then it can be express as:

$$\begin{aligned} E_1 < \langle \psi_2 | \hat{H}_1 | \psi_2 \rangle &= \int v_1(r) n(r) dr + \langle \psi_2 | (T + U) | \psi_2 \rangle \\ &= E_2 + \int \big[v_1(r) - v_2(r) \big] n(r) dr \end{aligned} \tag{2.18}$$

Similarly,

$$E_2 \leq \langle \psi_1 | H_1 | \psi_1 \rangle = E_1 + \int \big[v_2(r) - v_1(r) \big] n(r) dr \tag{2.19}$$

On solving the equation (2.18) and (2.19), we obtained that,

$$E_1 + E_2 < E_2 + E_1 \tag{2.20}$$

This equation 2.20 represents that, there is no possibility of two different external potentials with differences more than constant. It gives rise to the same non-degenerate ground state charge density, which uniquely determines the external potential within a constant.

2.2.2.2 Second Hohengberg-Kohn Theorem

According to this theorem, the exact ground state energy $E_0(n)$ of a system with an external potential $V_{ext}(r)$ is given by the global minimum value of the energy functional $E\big[n(r)\big]$, and the density that minimizes the functional is the ground state density $n_0(r)$. It is also considered an HK variational principle.

By using the principles of Lagrangian multiplier, we can write,

$$\delta \left\{ E - \mu \left[\int n(r) dr - N \right] \right\} = 0 \tag{2.21}$$

On solving the undetermined multiplier μ, we obtain the Euler Lagrange equation:

$$\begin{aligned}\mu &= \frac{\delta E\left[n(r)\right]}{\delta n(r)} \\ &= V_{ext}(r) + \frac{\delta F n(r)}{\delta n(r)}\end{aligned} \tag{2.22}$$

Here, μ is the chemical potential. Although the Hohengberg-Kohn Theorem set up the fundamental framework for DFT, it still remains a challenge to compute the universal functional and actual ground state density of the system.

2.2.3 Kohn-Sham Formalism

W. Kohn and L. Sham [33] established the application of DFT in computational modern physics and chemistry in 1965 by introducing the idea of atomic orbitals to calculate accurate kinetic energy [34].

It is the minimizing condition of the Hohenberg-Kohn theorem. As we know that, Energy function $E\left[n(r)\right]$ is related to external potential V_{ext} as [35]:

$$E\left[n(r)\right] = F\left[n(r)\right] + \int n(r)V_{ext}(r)dr \tag{2.23}$$

where,

$F\left[n(r)\right] = T\left[n(r)\right] + V_{ext}\left[n(r)\right]$

$F\left[n(r)\right]$ = universal constant i.e doesn't depend upon external potential.

In order to solve this $E\left[n(r)\right]$, we consider the variational method with ground state density $n(r)$.

$$n(r) = \sum_i \Phi_i^*(r)\Phi_i(r) \tag{2.24}$$

where $\Phi_i(r)$ refers to the number of orbitals and i runs from 1 to N.

Then, the electron density becomes:

$n_o(r) = \sum_i \Phi^*(r)\Phi(r)$

When kinetic energy functional of the non-interacting system, $\left[T_S(n)\right]$ is added in both sides of the equation 2.23, we get

$$E\left[n(r)\right] + T_s(n) = F\left[n(r)\right] + T_s(n) \int n(r)V_{ext}(r)dr$$

$$E\left[n(r)\right] = T_s(n) + \left\{T(n) - T_s(n) + v(n)\right\} + \int n(r)V_{ext}(r)dr \tag{2.25}$$

On introducing the Hartee expression on both sides of equation 2.25 and solving this equation, we get

$$E(n) = T_s(n) + E_{xc}(n) + \frac{e^2}{2}\int\int \frac{n(r)n(r'drdr')}{|r-r'|} + \int n(r)V_{ext}(r)dr \tag{2.26}$$

Thus, the exchange-correlation energy function is:

$$\begin{aligned} E_{xc}(n) =& \{T(n) - T_s(n) + V(n) - \frac{e^2}{2}\int\int \frac{n(r)n(r')}{|r-r'|}drdr'\} \\ &= F_{HK}(n) - \frac{e^2}{2}\int\int \frac{n(r)n(r')}{|r-r'|}drdr' \end{aligned} \tag{2.27}$$

where, $F_{HK} = T(n)+V(n)$

In order to minimize the functional $E_{xc}(n)$ with respect to n, we apply the equation 2.26 with respect to particle density,

$$\begin{aligned} \frac{\delta E(n)}{\delta n(r)} &= \frac{\delta T_s(n)}{\delta n(r)} + \frac{\delta E_{xc}(n)}{\delta n(r)} + e^2\int \frac{n(r')}{|r-r'|}dr' + V_{ext}(r) \\ &= \frac{\delta T_s(n)}{\delta n(r)} + V_{xc}(n) + e^2\int \frac{n(r')}{|r-r'|}dr' + V_{ext}(r) \end{aligned} \tag{2.28}$$

also,

$$\frac{\delta T_s(n)}{\delta n(r)} + V_{ks}(r) = 0 \tag{2.29}$$

where,

$V_{xc}(n) = \frac{\delta E_{xc}(n)}{\delta n(r)}$

$V_{ks}(r) = V_{ext}(r)+ V_{xc}(r) + V_{coulomb}(r)$

At last, Applying the variational principle of the energy functional of 2.26 leads to the Kohn Sham equation:

$$\left[-\frac{\hbar}{2m} + V_{ks}\right]\phi_i(r) = E_i\Phi_i(r) \tag{2.30}$$

2.2.4 Exchange-Correlation Functional

LDA, GGA, HSE, SCAN, and many other functions have been developed to explain the various features of the materials. Among them, LDA, GGA, and DFT+U are used in our research work in order to solve the strongly correlated behavior of ZnO. Mathematically, exchange-correlation can be expressed as:

$$E_{xc}\left[n(r)\right] = \int n(r)E_{xc}(r)dr \tag{2.31}$$

This process is repeated until it converges and obtains the expected minimum energy.

2.2.4.1 Local Density Approximation

To acquire the properties of metal, semiconductor, and insulator with the necessary accuracy, LDA approximation is employed. It can be formulated as:

$$E_{xc}^{LDA} = \int n(r)\epsilon_{xc}\big[n(r)\big]dr \tag{2.32}$$

Strong correlations exist in the ZnO system. Therefore, as this approximation is not appropriate for our system, we used GGA-PBE.

2.2.4.2 Generalized Gradient Approximation

LDA's flaw is fixed by GGA-PBE, which is really an extension of LDA. This approximation was introduced by three scientists, Perdew, Burke, and Ernzerhof in 1996. Here, in GGA-PBE, the exchange-correlation is the function of electron density and its gradient [6]. It can be stated as follows:

$$E_{xc}^{GGA} = E_{xc}\big[\rho(r), \nabla\rho(r)\big] \tag{2.33}$$

2.2.4.3 meta-Generalized Gradient Approximation

For geometries and energies of variously-bonded materials, including covalent, metallic, ionic, hydrogen, and van der Waals bonds, the recently developed non-empirical strongly constrained and appropriately normed meta-GGA SCAN significantly outperforms LDA and the standard Perdew-Burke-Ernzerhof at comparable efficiency.
It describes the laplacian-based electron density as a function of exchange-correlation. It has the following mathematical expression:

$$E_{xc}^{mGGA} = E_{xc}\big[\rho(r), \nabla\rho(r), \nabla^2\rho(r)\big] \tag{2.34}$$

SCAN may therefore be helpful even for the soft stuff. Often, at almost GGA cost, SCAN meets or exceeds the accuracy of a computationally expensive hybrid functional [36]. So, it is anticipated that SCAN will have a significant effect on materials science.

2.2.4.4 Hubbard U potential

DFT+U was designed to address these flaws because LDA and GGA-PBE were unable to calculate the approximation value. This technique is used to widen the band gap and

adjust for self-interaction and localized $d + f$ electrons and for p- electrons (sometimes), which closely matches experimental data [6]. Recently, it is referred to as LDA+U or GGA+U, and it may be expressed mathematically as.

$$E_{LDA+U}\left[n(r)\right] = E_{LDA}\left[n(r)\right] + E_U\left[n(r)\right] - E_{dc} \tag{2.35}$$

where, $n(r)$ = Probability of electron density

E_U = Hubbard energy

E_{dc} = double counting correction energy

Chapter 3

Details of Simulation

3.1 General Consideration

This chapter mainly covers our simulation work and the computation-related software. For first-principles calculations, we employed the plane wave basis set, PAW based on the VASP software package. In this section, we'll talk about how density functional theory can be used to optimize a number of parameters. Additionally, we discuss VESTA and Xmgrace, which are important resources for deciphering crystal structures and are incredibly helpful for examining the input and output files obtained during optimization. Additionally, we discuss the different codes and their purposes in our work.

3.2 Softwares Used

3.2.1 VASP

VASP stands for Vienna Ab initio Simulation Package. This package is used for quantum mechanical calculations. When using the Hartree-Fock (HF) approximation or density-functional theory (DFT), VASP solves the Kohn-Sham (KS) equations in order to approximate the solution to the many-body Schrödinger problem. There are also hybrid functionals that combine the Hartree-Fock method with density-functional theory. Additionally, VASP offers Green's functions approaches based on the many-body perturbation theory. For instance, the GW technique, the random-phase approximation, the second-order Miller-Plesset equations, the Bethe-Salpeter equations, and more [2].

Figure 3.1: Logo of VASP [2]

- **Input files**

  POSCAR: It consists of the system's ionic locations and lattice geometry, which were employed in the calculation.

  INCAR: It includes the algorithms and sets the various tags that pave the appropriate distinction for expected output.

  KPOINTS: It includes K-points.

  POTCAR: It contains the pseudo-potential for each component that is available and used in our calculation.

- **Output files :**

  Different outputs, such as CHG, CHGCAR, CONTCAR, DOSCAR, EIGENVAL, IBKPT, OSZICAR, PCDAT, OUTCAR, and others, are visible in the corresponding folder after the completion of our calculation.

  CONTCAR is changed to POSCAR for the SCF computation after relaxing. Further calculations, including BAND and DOS, are performed using WAVECAR and IBZKPT. Furthermore, we use OUTCAR, vaspout.h5, and vasprun.xml to extract our final data.

3.2.2 VESTA

VESTA is a 3D visualization tool for crystal morphologies, and volumetric data i.e. electron/nuclear densities, and structural models. Crystal faces, volumetric data, and several structural models are superimposed on the same graphic area [37]. Linux, Mac

OS X, and Windows all support VESTA. It is provided for free to non-commercial users. It reads *.vasp, *.cif, *.vesta, and many more extension files.

The key purposes for which we employed this software were the production of monolayers, doping, and obtaining the primary input i.e. POSCAR, for our calculations. Additionally, it makes use of a GUI to set atom positions and visualize the molecular structure.

3.2.3 VASPKIT

We introduce the VASPKIT, a command-line tool that seeks to offer a robust and intuitive interface for high-throughput analysis of a range of material properties from the raw data generated by the VASP code. Primarily, it consists of pre- and post-processing modules. The first module's purpose is to create and manipulate input files, such as symmetry analysis, supercell transformation, and k-path generation for a specific crystal structure. This module's purpose is to extract and analyze raw data related to elastic mechanics, electronic structure, charge density, electrostatic potential, linear optical coefficients, wave function graphs in real space, and other topics [38]. It is convenient to utilize the interactive user interface or the command line to run this application.

3.2.4 Xmgrace

A fairly simple Linux operating system comes with the helpful charting of 2D graphs basically known as Xmgrace. We can plot the output of VASP through this software which is widely used for the comprehension and analytic study of our output data.

3.3 Computational Details

Using VASP software, we have conducted first-principle calculations to examine the structural stability, electrical, and magnetic characteristics of pristine ZnO and Al-doped ZnO monolayer, before and after adsorption of hydrogen cyanide(HCN), and hydrogen sulfide (H_2S). We employed the GGA-PBE, SCAN, and DFT+U (U_d, Zn = 10 eV, U_p, O = 7eV) [6] functionals to analyze the exchange-correlation effect of the system. We employed the plane wave basis set function, which has a cutoff energy of 520 eV, i.e. 1.3 folds of the maximum cut-off energy of an atom. $8 \times 8 \times 4$ k-points are used for the

Brillouin zone for all the calculations except DOS ($22 \times 22 \times 11$). The models of $3 \times 3 \times 1$ supercells of ZnO monolayer with an Al atom in place of one Zn atom are considered. Later, hydrogen sulfide (H_2S) and hydrogen cyanide (HCN) were adsorbed into the system. Projected Augmented wave, PAW considers the valance electrons $4s^2 3d^{10}$ for Zn, $2s^2 2p^4$ for O, $3s^2 3p^1$ for Al, $1s^1$ for H, $2s^2 2p^2$ for C, $2s^2 2p^3$ for N, and $3s^2 3p^4$ for S whereas other inner electrons remain isolated within ions' environment. Spin polarization is employed for all of the calculations.

Chapter 4

Results and Discussion

4.1 General Consideration

In this chapter, our key findings and their interpretations are presented. In our work, spin-polarized DFT calculations were successfully computed in order to determine the structural, electronic, and magnetic properties of the 3 × 3 × 1 supercells of ZnO. Moreover, we studied the different properties of the Al-doped ZnO mono-layer using functionals like PBE, SCAN, and DFT+U. Finally, band structure and DOS calculations were carried out to comprehend the change in electrical and magnetic properties brought about by the absorption of HCN and H_2S molecule in mono-layer and Al-doped ZnO. At last, we compared our findings to available experimental and theoretical data from earlier studies that had been published.

4.2 Structural Properties

The bulk structure, taken from the material projects, is relaxed as the first and foremost step of theoretical research. We used non-magnetic, hexagonal wurtzite ZnO with space group $p6_3mc$ [39]. We primarily concentrated on geometrical optimization, ionic optimization, energy optimization, and ground-state structure optimization for relaxation. We considered the lattice parameters, k-points, cut-off energy, and other factors to determine the system's stability. The lattice constant of ZnO is a = 3.249 $\mathring{A}$ and c/a = 1.602 $\mathring{A}$ [40].

Convergence test of K-points

While doing an SCF calculation to determine the energy, the Brillouin zone has to be sampled, which is basically known as the K-points. These K-points specify the preciseness of Brillouin Zone sampling. In Figure 4.1, it is clearly seen that the total energy becomes almost constant when the K-points, K=8. Hence, we employed $8 \times 8 \times 4$ K-points for all the calculations except the Density of state calculation ($22 \times 22 \times 11$). However, high symmetric K-points (Γ-M-K-Γ) are used in Band calculation.

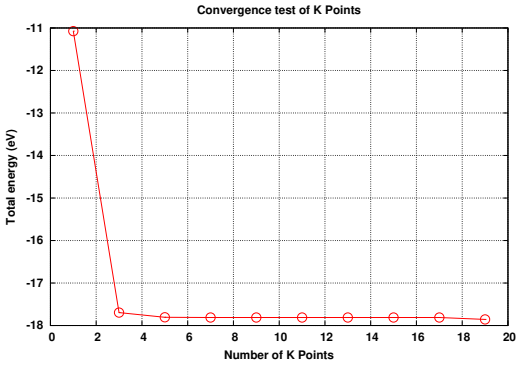

Figure 4.1: Total energy vs number of k-Points for our system, ZnO.

Table 4.1 shows the optimal lattice parameter, bond length, and formation energy (eV), which were derived using various functions. The maximum feasible lattice constant is produced using PBE functional, and the lattice constant optimized using SCAN gives results nearly identical to the experimental value. Additionally, table 4.1 also provides information about the optimized lattice constant for $3 \times 3 \times 1$ ZnO mono-layer and Al-doped ZnO mono-layer. Thus obtained lattice constant and bond length are identical to the former work [21].

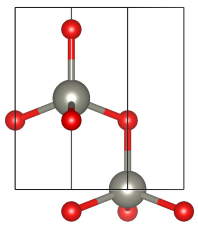

Figure 4.2: Relaxed bulk structure of ZnO

- **Structural properties of ZnO monolayer and $Al-$doped ZnO**

Figure 4.3 represents the non-relaxed and relaxed structure of ZnO monolayer and AL-doped ZnO mono-layer with their respective side and top views. After optimization, the optimized lattice constant and other different parameters are found equivalent to the previous work [6]. The different structural parameters are shown in table 4.1.

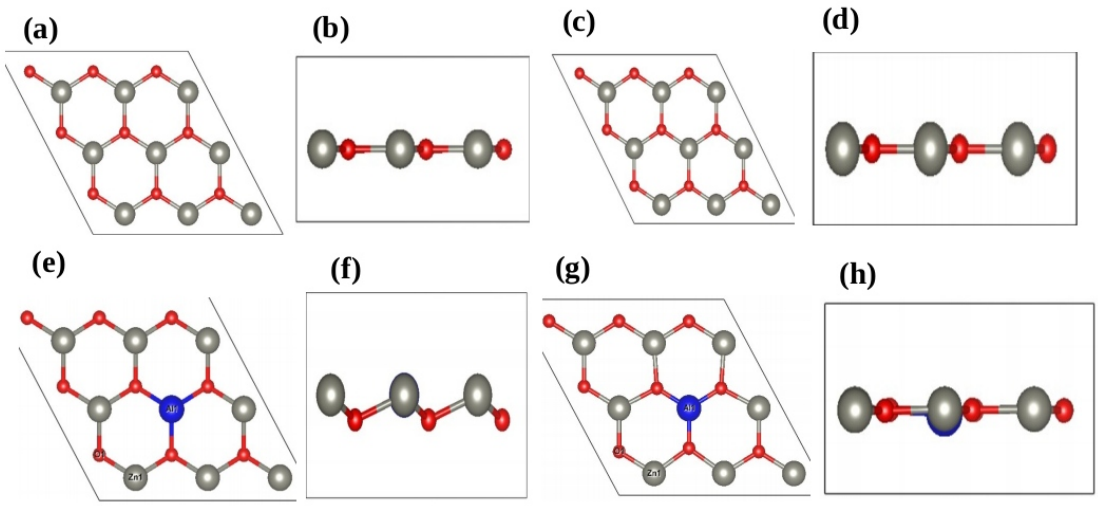

Figure 4.3: Structural parameters of $(3\times 3\times 1)$ ZnO and Al-doped ZnO monolayer:(a) unrelaxed ZnO side view (b) unrelaxed ZnO top view (c) relaxed side view (d) relaxed top view (e) unrelaxed Al-ZnO side view (f) unrelaxed Al-ZnO top view (g) relaxed Al-ZnO side view (h) relaxed Al-ZnO top view respectively.

- **Structural properties for HCN adsorbed ZnO mono-layer and Al-doped Zno**

  Figure 4.10 discloses the relaxed and non-relaxed structure of HCN adsorbed ZnO and Al-doped ZnO with their respective side and top view. The adsorption energy obtained after calculations is -2.27 eV, -2.31 eV, and -2.46 eV for PBE, SCAN, and DFT+U functional in HCN adsorbed ZnO. Similarly, the adsorbed energy for HCN adsorbed Al-doped ZnO is -14.88 eV, -18.21 eV, and -15.40 eV for PBE, SCAN, and DFT+U functionals respectively. Similarly, the optimized structural parameters are shown in the table 4.2, 4.3

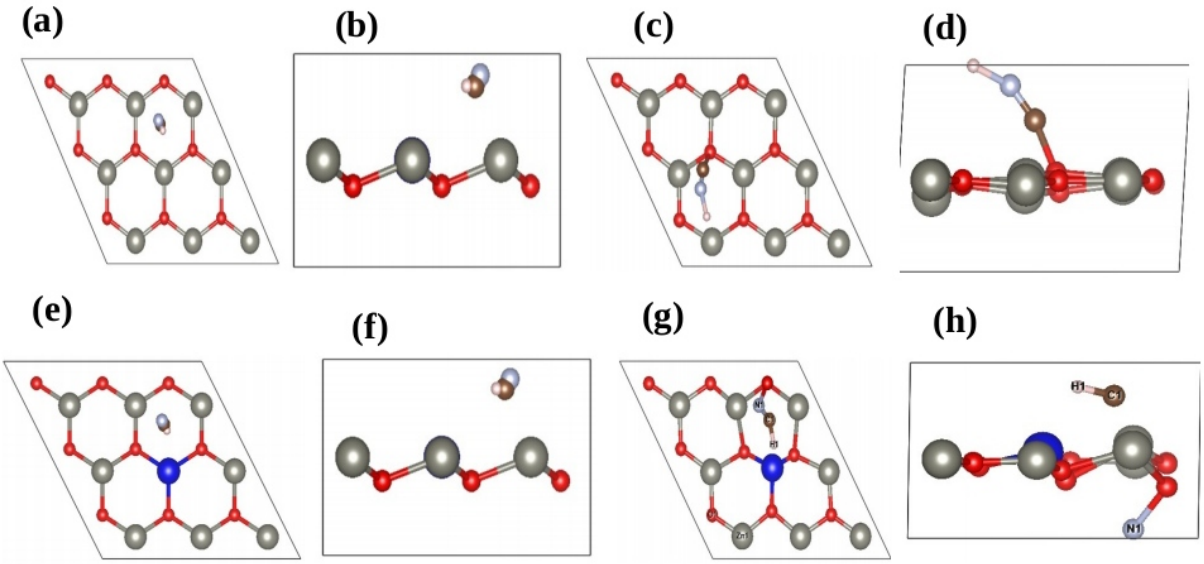

Figure 4.4: Structure of HCN adsorbed ZnO monolayer:(a)unrelaxed side view, (b) unrelaxed top view,(c) relaxed side view, and (d) relaxed top view and Structure of HCN adsorbed Al-doped Zno: (e) unrelaxed side view, (f) unrelaxed top view,(g) relaxed side view, and (h) relaxed top view.

- **Structural properties of H_2S adsorbed ZnO monolayer and Al-doped ZnO**

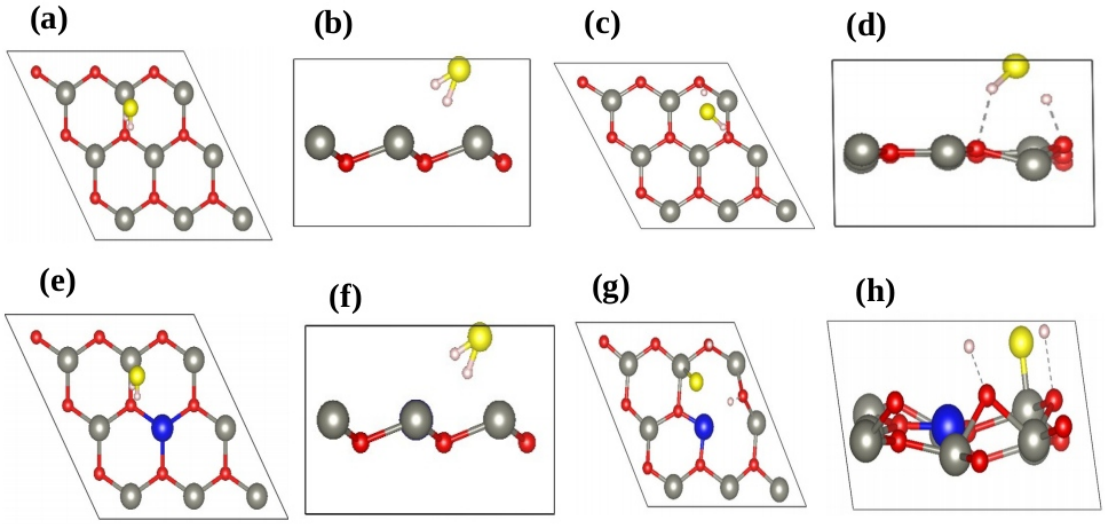

Figure 4.5: Structure of H_2S adsorbed ZnO monolayer: (a)unrelaxed side view, (b) unrelaxed top view,(c) relaxed side view, and (d) relaxed top view and Structure of H_2S adsorbed Al-doped Zno: (e) unrelaxed side view, (f) unrelaxed top view,(g) relaxed side view, and (h) relaxed top view.

Figure 4.5 shows the relaxed and unrelaxed structure of H_2S adsorbed ZnO monolayer and Al-doped ZnO with their respective side and top views. The adsorption energy thus calculated are -2.65 eV, -2.31 eV, and -2.46 eV and -8.80 eV, -7.48 eV, and -6.82 eV while using PBE, SCAN, and DFT+U functionals in H_2S adsorbed ZnO monolayer and Al-doped ZnO respectively. Similarly, the different structural parameter of H_2S adsorbed ZnO and Al-doped ZnO is shown in table 4.4, and 4.5.

Table 4.1: Optimized structural parameters for bulk ZnO, its $3 \times 3 \times 1$ mono-layer and Al-doped ZnO

Compound	Functional	a ($\mathring{A}$)	b=c ($\mathring{A}$)	bond length(Zn-O)$\mathring{A}$	Al-O $\mathring{A}$
Bulk	PBE	3.29	5.32	2.04	-
	SCAN	3.24	5.22	2.04	-
	DFT+U	3.09	4.97	2.04	-
Monolayer	PBE	4.59	9.88	2.04	-
	SCAN	3.49	9.70	2.04	-
	DFT+U	4.54	9.20	2.04	-
Al-ZnO	PBE	4.07	9.84	2.04	2.14
	SCAN	4.61	9.70	2.04	2.14
	DFT+U	4.09	9.24	2.04	2.14

Table 4.2: Structural properties of HCN adsorbed ZnO monolayer using different functionals.

					Bond length			
System	Functional	a	b	c	Zn-O	H-N	C-N	C-O
	PBE	9.88	9.78	5.09	2.04	1.2	1.79	1.97
$HCN - ZnO$	SCAN	9.78	9.79	4.66	2.04	1.2	1.79	1.97
	DFT+U	9.25	9.20	5.30	2.04	1.2	1.79	1.97

Table 4.3: Structural properties of HCN adsorbed Al-ZnO monolayer using different functional.

		Bond length							
System	Functional	a	b	c	Zn-O	H-N	C-N	C-O	Al-O
	PBE	9.87	9.76	5.16	2.04	1.2	1.79	1.97	2.11
$HCN - AlZnO$	SCAN	9.07	9.25	4.91	2.04	1.2	1.79	1.97	2.11
	DFT+U	9.22	9.30	5.16	2.04	1.2	1.79	1.97	2.11

Table 4.4: Structural properties of H_2S adsorbed ZnO monolayer using different functionals.

		Bond length						
System	Functional	a	b	c	Zn-O	H-S	H-O	Zn-S
	PBE	9.85	9.79	5.51	2.04	1.43	2.1	2.8
$H_2S - ZnO$	SCAN	9.68	9.71	5.44	2.04	1.43	2.1	2.8
	DFT+U	9.21	9.21	5.50	2.04	1.43	2.1	2.8

Table 4.5: Structural properties of H_2S adsorbed Al-ZnO monolayer using different functionals.

		Bond length($\mathring{A}$)						
System	Functional	a	b	c	Zn-O	Zn-S	H-O	Al-O
	PBE	9.82	9.41	4.91	2.04	2.80	2.10	2.11
$H_2S - AlZnO$	SCAN	10.0	9.48	5.07	2.04	2.80	2.10	2.11
	DFT+U	9.32	8.98	4.88	2.04	2.80	2.10	2.11

4.3 Electronic Properties

4.3.1 Electronic properties of ZnO monolayer

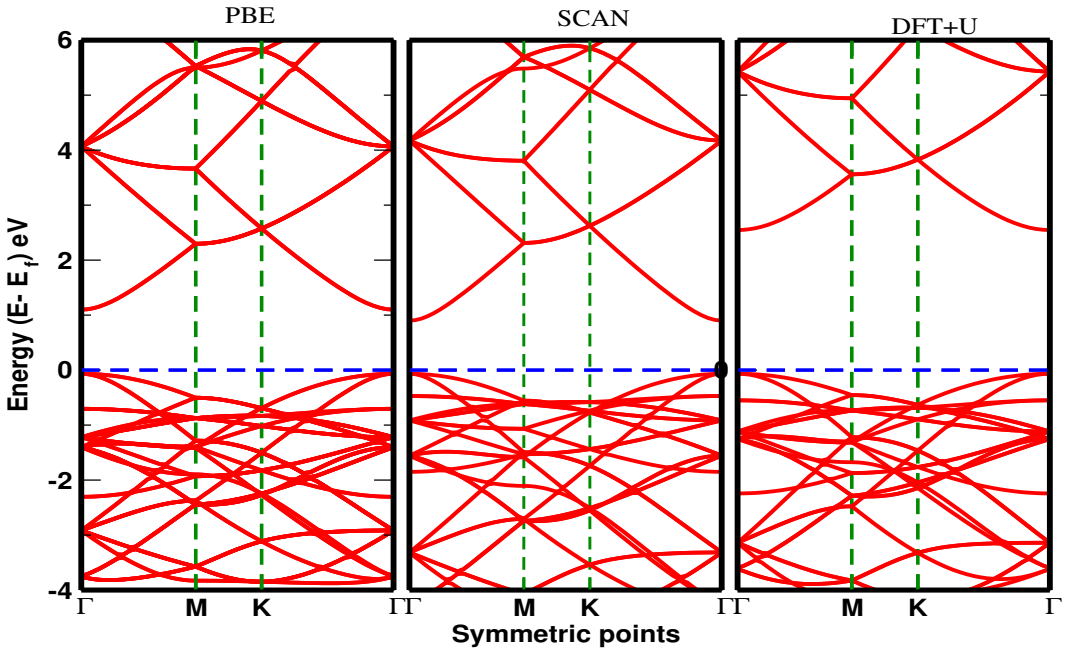

Figure 4.6: Band structure of $3 \times 3 \times 1$ monolayer of ZnO using various exchange-correlation functionals

Figure 4.6 depicts the band structure of a pristine ZnO monolayer ($3 \times 3 \times 1$). The fermi energy level, which is set to 0 eV, is shown by the horizontal dot line. Similarly, the high symmetric points are represented by the vertical dot lines. The valance band maximum and conduction band minimum lie on the same k-points, so, the calculated band gap is direct. Figure 4.6 depicts the band structure, as determined by PBE, The second one is based on SCAN, and thus calculated band energy is 1.17 eV and 0.97 eV, which is comparatively less than the experimental value of 3.4 eV [6]. Due to the quantum bound effect, the aforementioned two functionals provide the underestimated band energy. However, DFT+U helps to widen the band energy, when the potential is applied. For our work, we employed $U_d, Zn = 10$ eV, $U_p, O = 7$ eV potential and succeeded in getting the band energy of 2.61 eV, which is more precise and accurate to experimental value and it vividly agrees with the earlier work [6, 41].

Figure 4.7 depicts the information about the Band and DOS of the pristine ZnO monolayer, which is obtained by employing the GGA-PBE functional. The horizontal dot line implies the fermi level, which is set to 0 eV. The Fermi energy thus obtained is -1.68 eV.

The band and DOS structure are in good agreement with each other. It is discovered that the highest DOS is 40 states/eV when the energy level is -1 eV in the valance band.

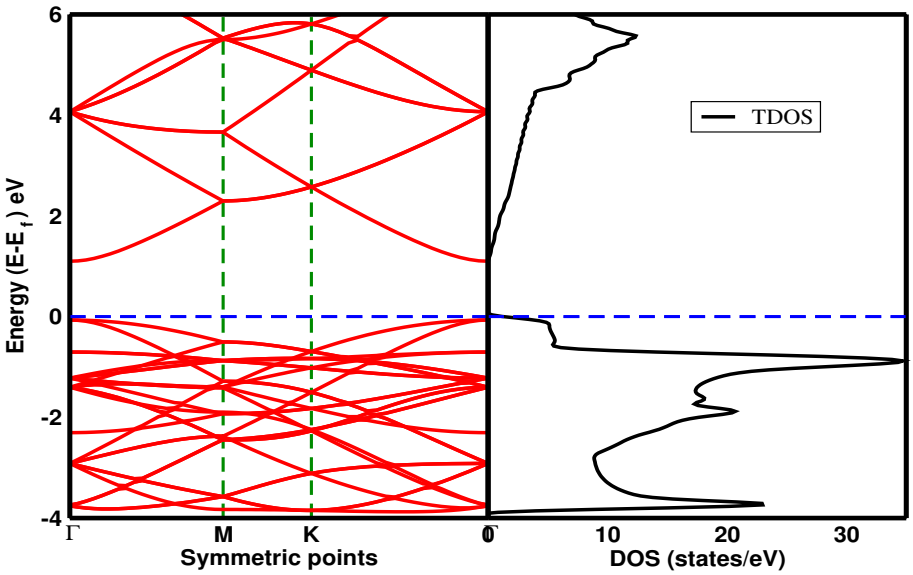

Figure 4.7: Band and DOS of pristine ZnO monolayer, which is extracted using PBE functional

Figure 4.8 depicts the information about the Band and DOS of the pristine ZnO monolayer, obtained by employing mGGA-SCAN functional. The horizontal dash line implies the Fermi level, which is set to 0 eV. Thus, the calculated Fermi energy is - 0.59 eV. It is clearly seen that the band and DOS are in good agreement with each other. The highest density of states is obtained at about -1 eV, which is around 25 states/eV.

Figure 4.9 represents the information about the Band and DOS of the pristine ZnO monolayer, obtained by employing the DFT+U functional. The Fermi level, represented by a horizontal dash line is set to 0 eV. Thus, the obtained Fermi energy is -2.01 eV. Similarly, the band and DOS are in good agreement with each other. The highest density of states is found near -1 eV, which is around 16 states/eV.

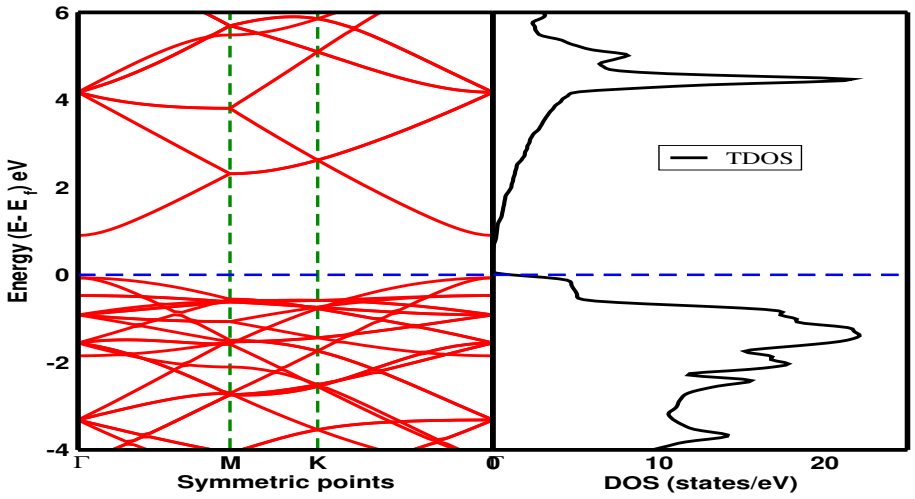

Figure 4.8: Band and DOS of pristine ZnO monolayer, which is extracted using mGGA-SCAN functional

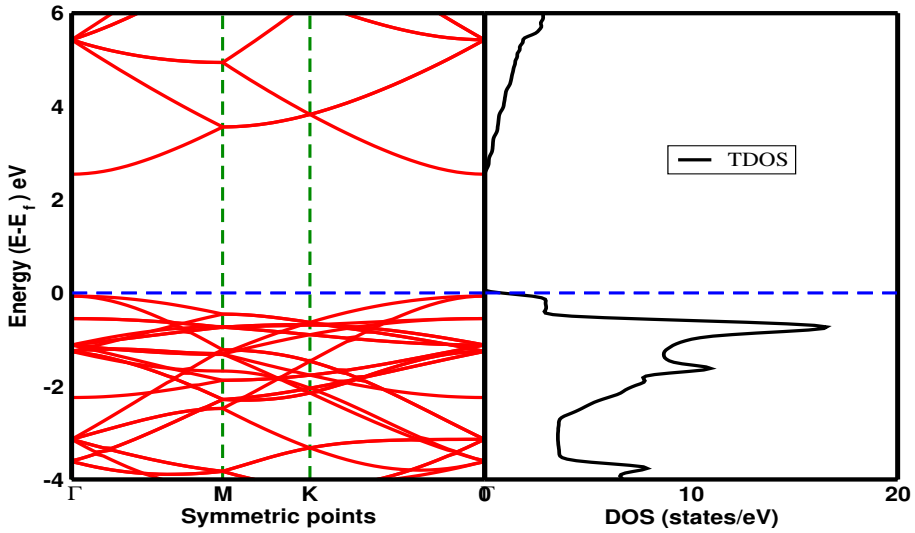

Figure 4.9: Band and DOS of pristine ZnO monolayer, which is extracted using DFT+U functional

The projection of the valance orbitals of each atom in the DOS using various functionals is shown in figure 4.10 where the vertical red dash line represents the fermi level, which is set to 0 eV. The orbital contributions of the Zn-3d, Zn-4s, O-2s, and O-2p are shown in the respective figures. When PBE and SCAN functionals are employed the highest peak in the TDOS is discovered near -5 eV in the valance band, which is contributed by Zn-3d orbitals. Furthermore, the second highest peak is found near the fermi level at about -1 eV, which is due to the O-2p orbital. However, when DFT+U is employed the highest peak in TDOS is obtained near -1 eV, which is highly contributed

by O-2p and Zn-3d (partially contributed). Moreover, another peak is seen near -4 eV, which is due to Zn-4s, and O-2p.

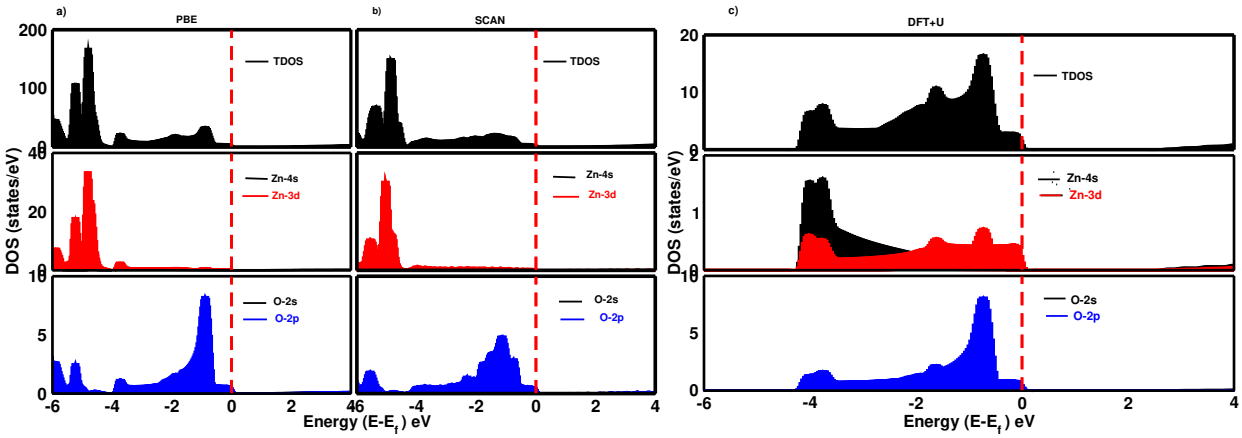

Figure 4.10: PDOS of ZnO monolayer by using different functional: (a) PBE, (b) SCAN, and (c) DFT+U

4.3.1.1 Magnetic properties

In Figure 4.11, 4.12, and 4.13 the vertical dash line represents the fermi level, which is set at 0 eV. After the calculation of the DOS with spin polarization by employing all the functional i.e. PBE, SCAN, and DFT+U, we were unable to detect any changes between spin up and spin down as we found symmetry between spin up and spin down in DOS. We may therefore assert that the system under examination is non-magnetic i.e. the magnetic moment is zero.

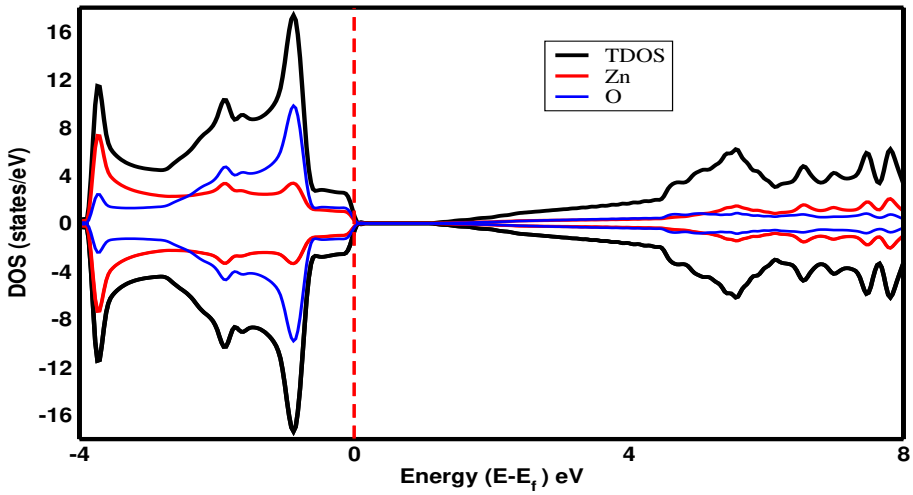

Figure 4.11: Spin polarised DOS of *ZnO* monolayer, which is obtained by PBE functional

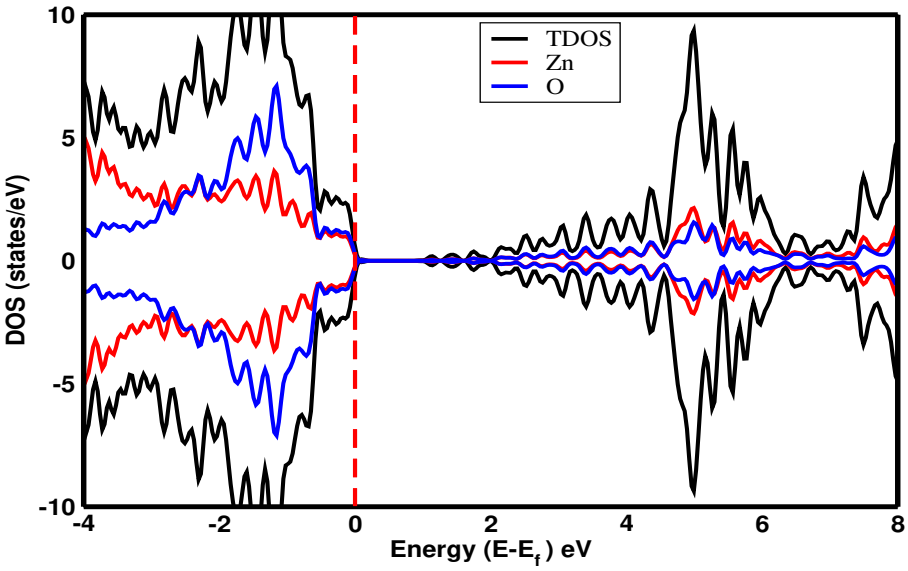

Figure 4.12: Spin polarised DOS of *ZnO* monolayer, which is obtained by SCAN functional

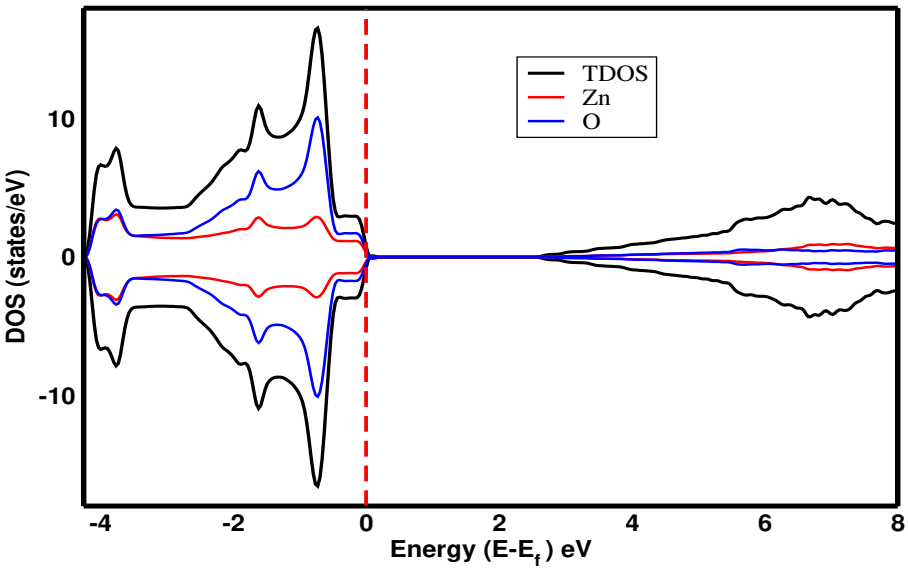

Figure 4.13: Spin polarised DOS of *ZnO* monolayer, which is obtained by DFT+U functional

4.3.2 Electronic properties of *Al*-doped *ZnO*

The band structure of an Al-doped ZnO monolayer, in which an Al atom has replaced one Zn atom, is shown in Figure 4.14. When Al is doped in ZnO, the energy states from the conduction band shift downward into the valance band, which implies that the conductivity of the system is considerably increased as compared to the pristine one. When pristine ZnO is doped with Al then the carrier concentration rises at the bottom of the conduction band due to the production of shallow states near Fermi level [21].

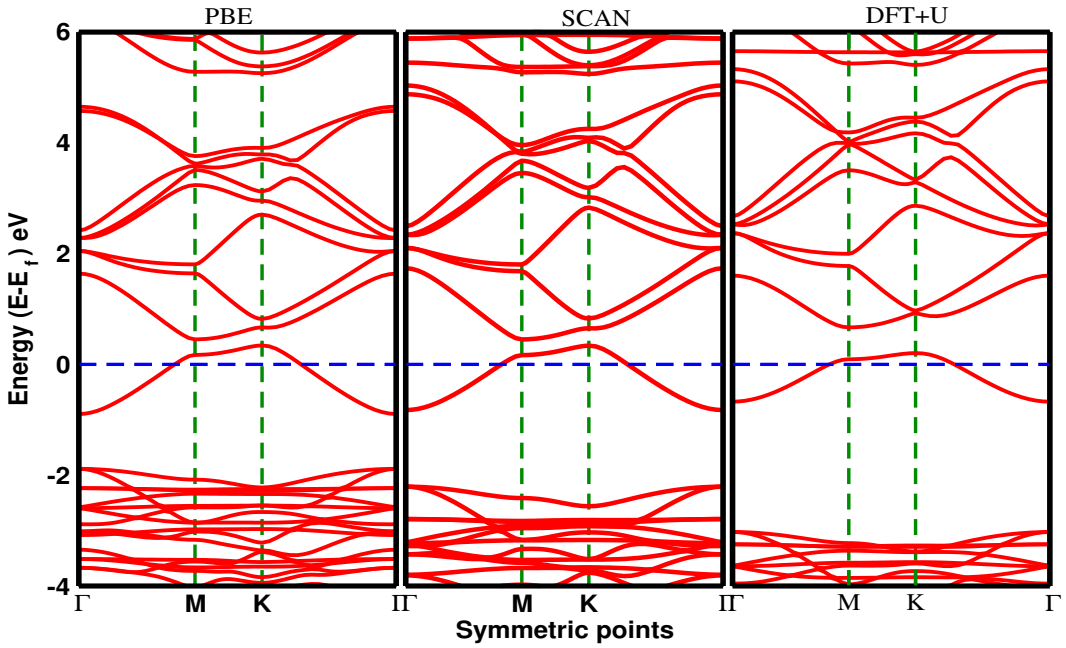

Figure 4.14: Band structure of Al-doped ZnO monolayer using various exchange-correlational functional

The band gaps thus obtained are 0.07 eV, 0.06 eV, and 0.05 eV by using PBE, SCAN, and DFT+U respectively. When Ga and In are doped to ZnO then both of them show a similar nature, which signifies our work agrees with the previous work [42].

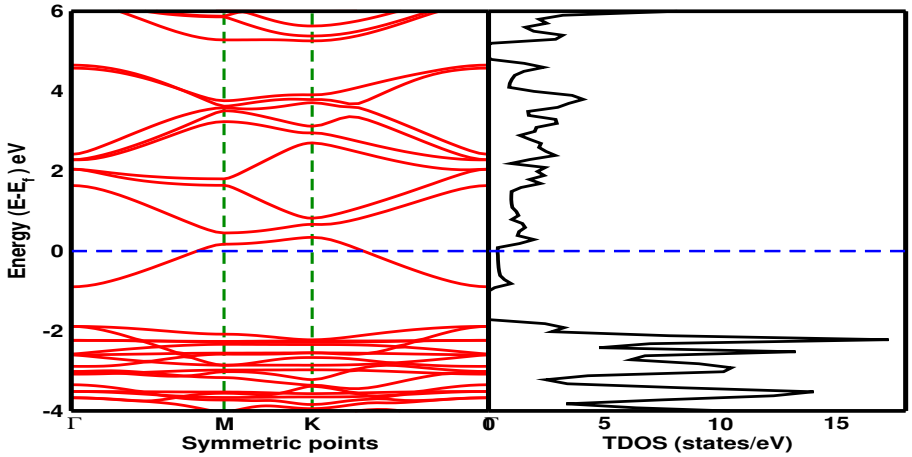

Figure 4.15: Band and DOS structure of Al-doped ZnO, which is extracted by employing PBE functional

The band and DOS of Al-doped ZnO are shown in Figures 4.15, 4.16, and 4.17, which are obtained by using the PBE, SCAN, and DFT+U functional. The Fermi level, adjusted to 0 eV, is indicated by the blue horizontal dashed line. Bands and DOS appear

to be in good agreement with one another in all three cases. For PBE and SCAN, the maximum density of states is discovered near the energy level -2 eV, whereas the density of states is found maximum at about the energy level -3 eV for DFT+U. Thus, for PBE, SCAN, and DFT+U, respectively, the greatest state densities obtained were 18 states/eV, 38 states/eV, and 15 states/eV.

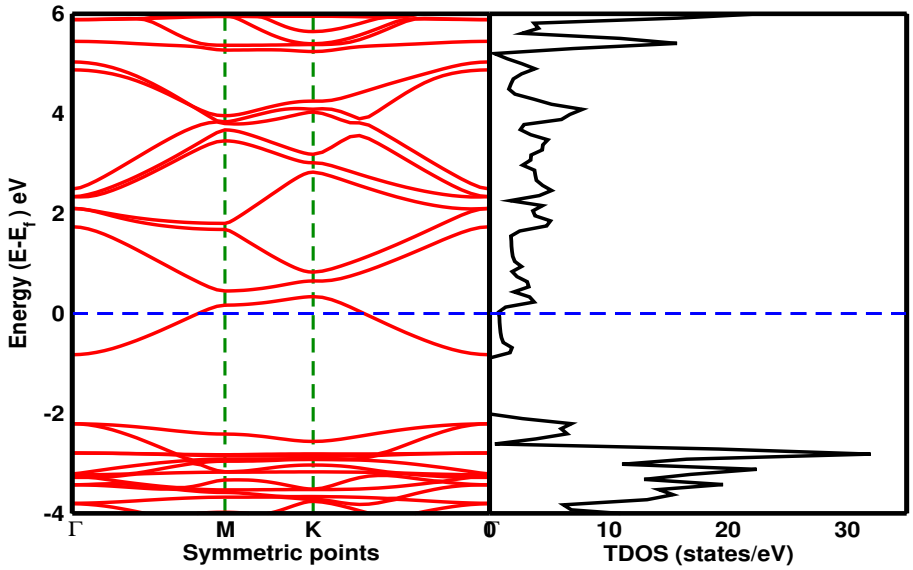

Figure 4.16: Band and DOS structure of Al-doped ZnO, which is extracted by employing SCAN functional

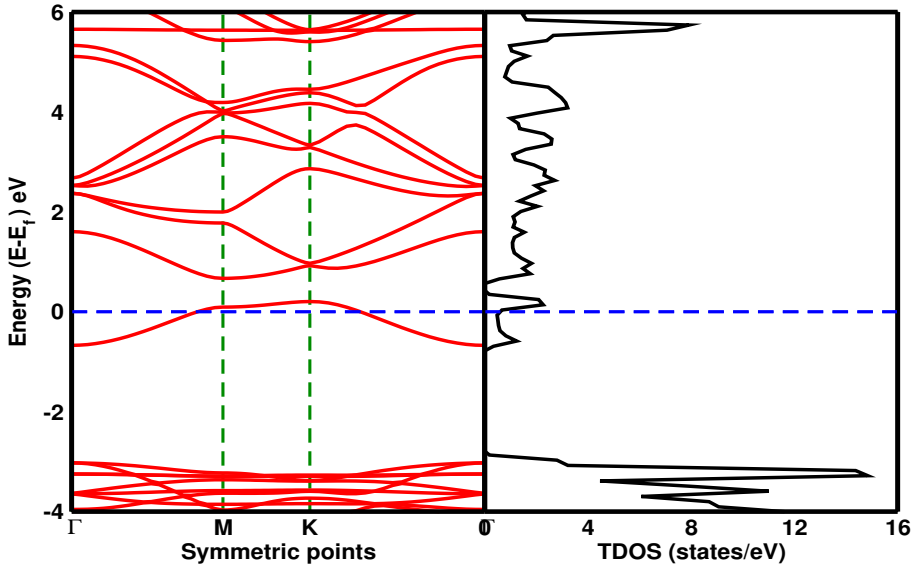

Figure 4.17: Band and DOS structure of Al-doped ZnO, which is extracted by employing DFT+U functional

The projection of the valance orbitals of each atom in the DOS using various func-

tionals is shown in figure 4.18 where the vertical red dash line represents the fermi level, which is set to 0 eV. The orbital contributions of the Zn-3d, Zn-4s, O-2s, O-2p, Al-3s, and Al-3p are shown in the respective Figures. The peak in the TDOS is obtained between -2 eV and -5 eV in the valance band, which is due to Al-3p, Zn-3d, and O-2p orbitals in PBE functionals. Similarly, peaks found near 3 eV in the conduction band were formed due to the influence of O-2p, and Al-3p respectively. Furthermore, the peak near 3 eV in the conduction band is partially contributed by Zn-4s. However, in SCAN, and DFT+U functional peaks are found in between -4 eV and -6 eV, which are formed due to the Al-3p, Zn-3d, and O-2p orbitals. On the other hand, we also found the peak in the conduction band from 1 eV to 4 eV. This is due to the contribution of Al-3p, and O-2p orbitals.

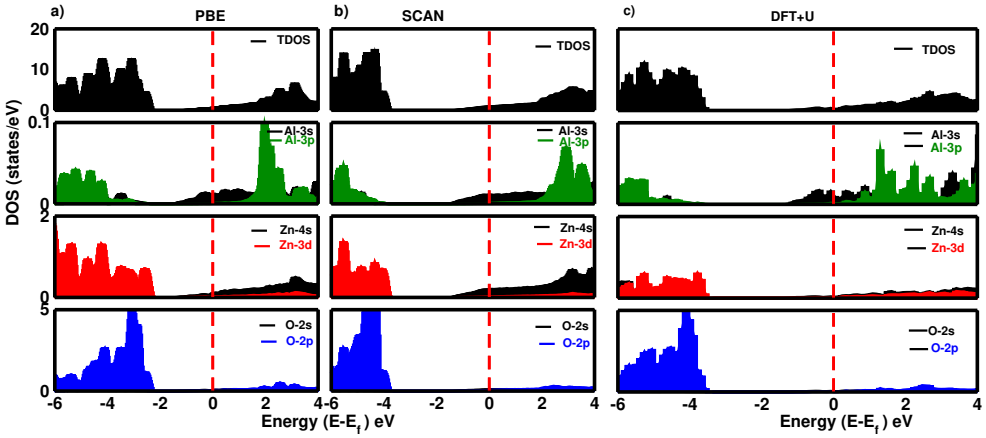

Figure 4.18: PDOS of *Al*-doped *ZnO*, which is discovered by employing different functional: (a) PBE, (b) SCAN, and (c) DFT+U

4.3.2.1 Magnetic Properties

In Figure 4.19 the vertical dash line represents the fermi level, which is set at 0 eV. After the calculation of DOS with spin polarization in Al-doped ZnO, we were unable to detect any change between spin up and spin down. We found symmetry between spin up and spin down in DOS. On calculating the magnetic moment, we obtained the magnetic moment zero for PBE, SCAN, and DFT+U. Moreover, It has been found that the magnetic moment is zero for all the functionals. Hence, we can assert that the system under study is non-magnetic.

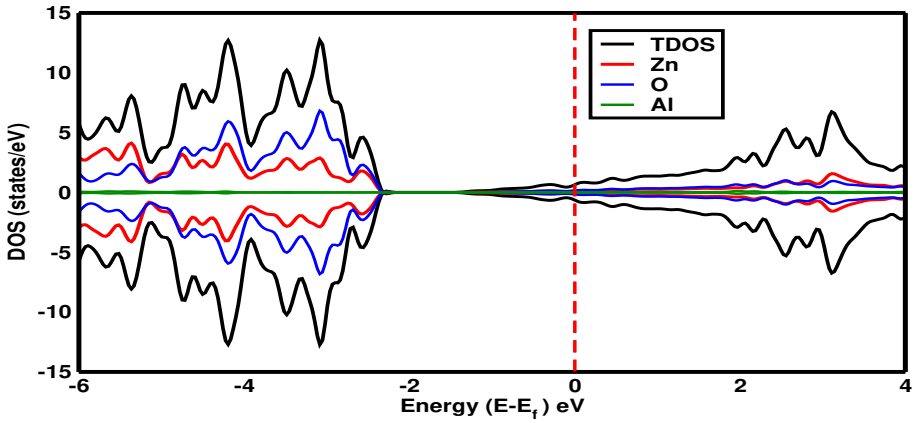

Figure 4.19: Spin polarised DOS of Al-doped ZnO monolayer, which is obtained by PBE functional.

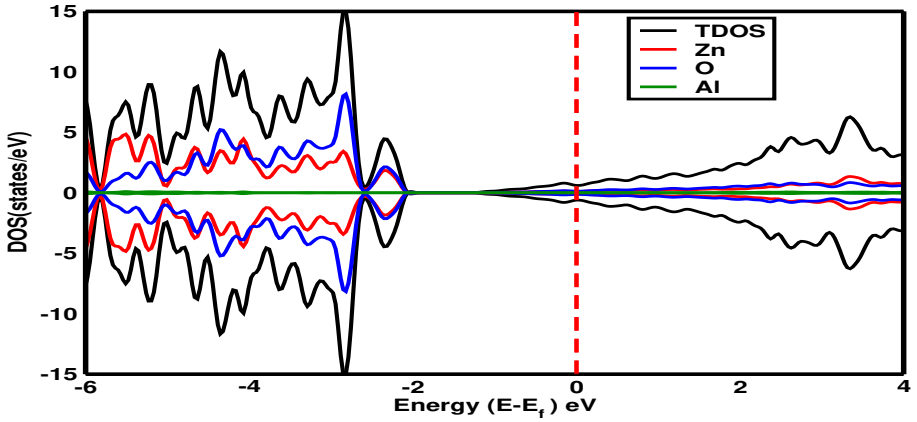

Figure 4.20: Spin polarised DOS of Al-doped ZnO monolayer, which is obtained by SCAN functional.

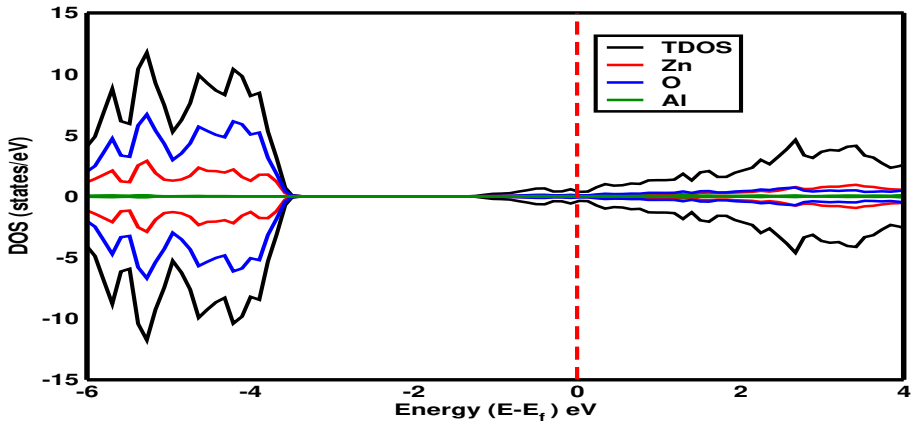

Figure 4.21: Spin polarised DOS of Al-doped ZnO monolayer, which is obtained by DFT+U functional.

4.3.3 Electronic properties of H_2S Adsorbed ZnO monolayer

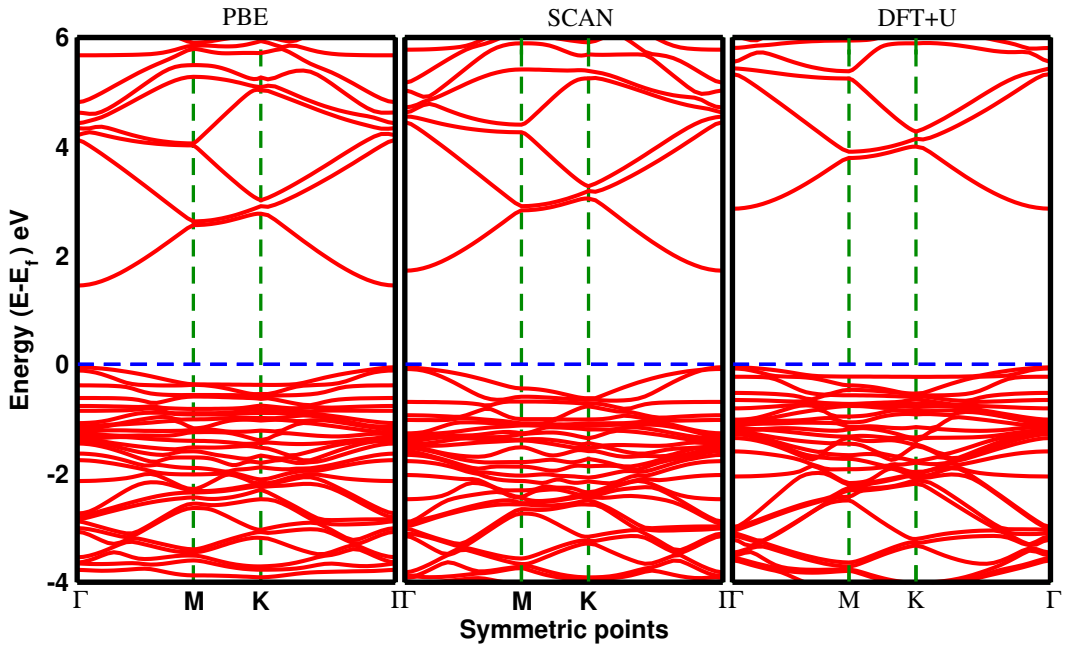

Figure 4.22: Band structures of H_2S adsorbed ZnO monolayer using different exchange-correlation functional

Figure 4.22 depicts the Band structure of H_2S adsorbed ZnO monolayer by employing three different exchange-correlation functional. The horizontal blue dot line signifies the fermi level, adjusted to 0 eV. Similarly, the vertical dot line represents the high symmetric points (Γ -M -K- Γ), which were used for band calculation. When H_2S is adsorbed in the pristine monolayer, then the band gap became wide as compared to the pristine one and we calculated 1.50 eV, 1.77 eV, and 2.91 eV band energy for PBE, SCAN, and DFT+U respectively. The calculated band is a direct band structure as the valance band maximum and conduction band minimum lie on the same k-points.

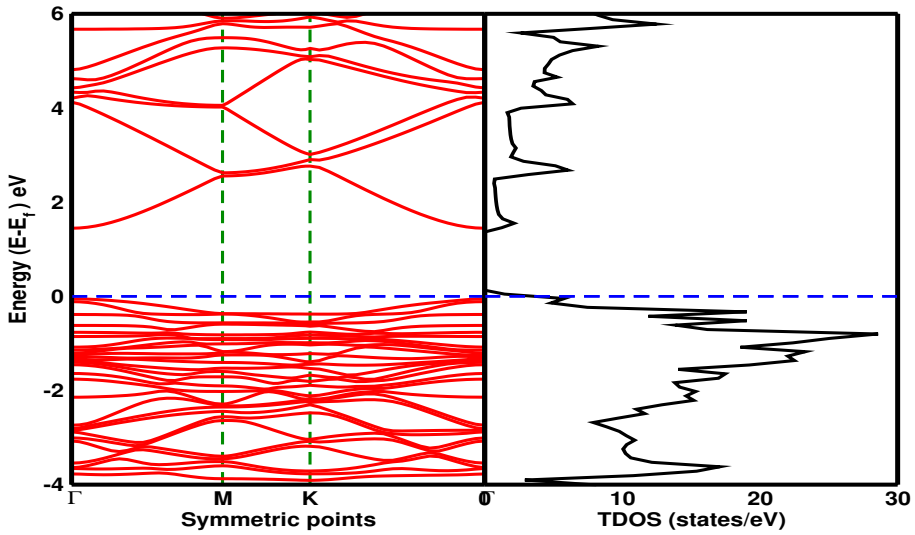

Figure 4.23: Band and DOS structure of H_2S adsorbed ZnO monolayer, which is extracted by employing PBE functional

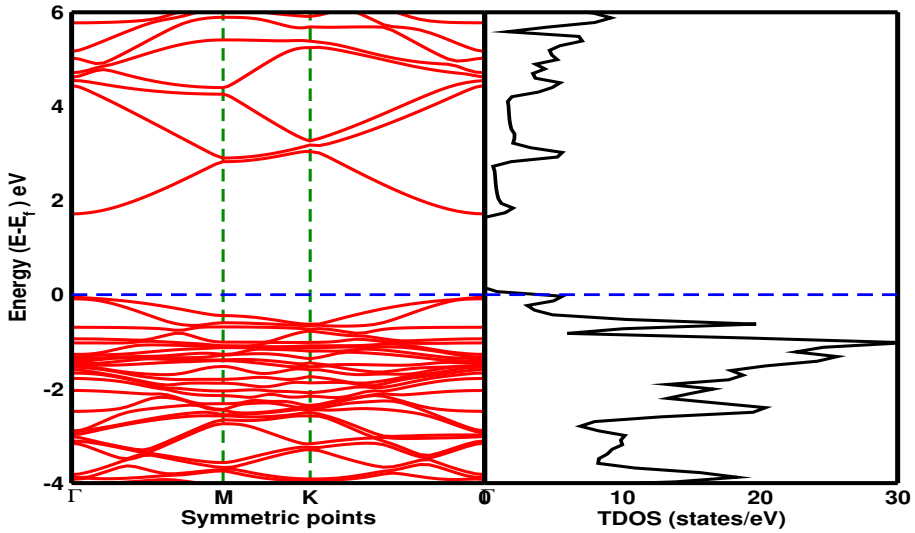

Figure 4.24: Band and DOS structure of H_2S adsorbed ZnO monolayer, which is extracted by employing SCAN functional

Using PBE, SCAN, and DFT+U functional, the band and DOS of the H_2S adsorbed Zno monolayer are shown in Figure 4.23, 4.24, 4.25. The Fermi level, set to 0 eV, is represented by the horizontal blue dashed line. Thus calculated Fermi energies for PBE, SCAN, and DFT+U functional are 1.83 eV, 1.77 eV, and 2.15 eV, respectively. The state's highest density is, respectively, 28 states/eV, 30 states/eV, and 27 states/eV near about Fermi energy -1 eV in all three cases.

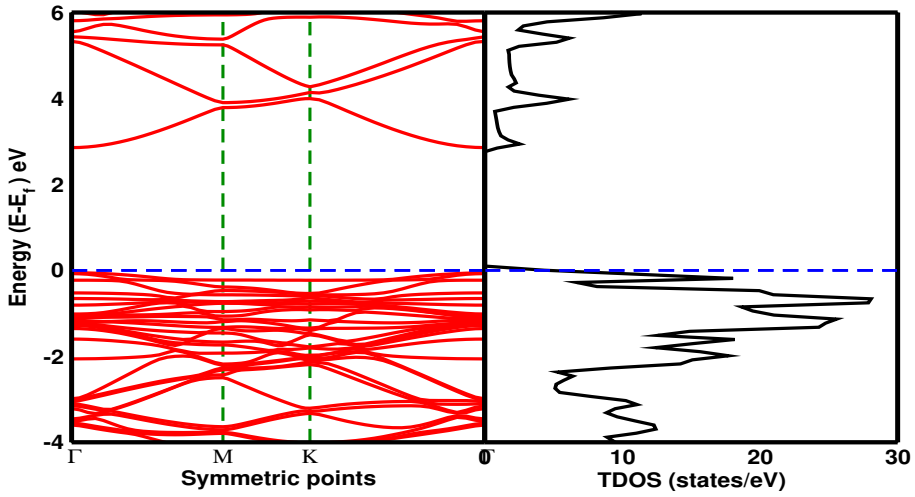

Figure 4.25: Band and DOS structure of H_2S adsorbed ZnO monolayer, which is extracted by employing DFT+U functional

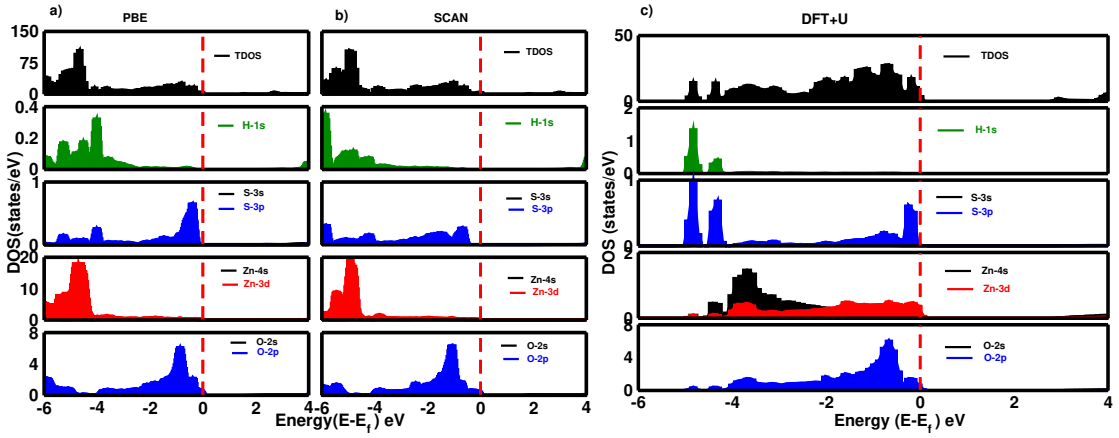

Figure 4.26: PDOS of H_2S adsorbed ZnO monolayer, which is obtained by using different functional:(a) PBE ,(b) SCAN , and (c) DFT+U.

The projection of the valance orbitals of each atom in the DOS using various functionals is shown in figure 4.26 where the vertical red dash line represents the fermi level, which is set to 0 eV. The orbital contributions of the Zn-3d, Zn-4s, O-2s, O-2p, H-1s, S-3s, and S-3p are shown in the respective Figures. The highest peak in the valance band of the TDOS is found near about -5 eV, which is due to Zn-3d, and H-1s orbitals in PBE functionals. Another peak is found near the Fermi level due to S-3p and O-2p orbitals. An almost similar pattern is seen for SCAN functional as well. However, On employing the DFT+U functional, peaks discovered near the -5 eV in the valance band are due to the H-1s and S-3p orbitals. Peaks near the Fermi level in TDOS are obtained due to S-3p, Zn-3d, and O-2p orbitals.

4.3.3.1 Magnetic properties

Figure 4.27, 4.28, and 4.29 depict the spin-up and spin-down density of states of the H_2S adsorbed ZnO monolayer, which is obtained by employing the three different functional, which are PBE, SCAN, and DFT+U respectively. On precisely studying the spin-up and spin-down nature of all the figures, we observed the symmetry between the up and down spin. Moreover, we computed the magnetic moment zero in PBE as well as other exchange-correlation functional i.e. SCAN, and DFT+U. Hence, we can assure the material under study is non-magnetic.

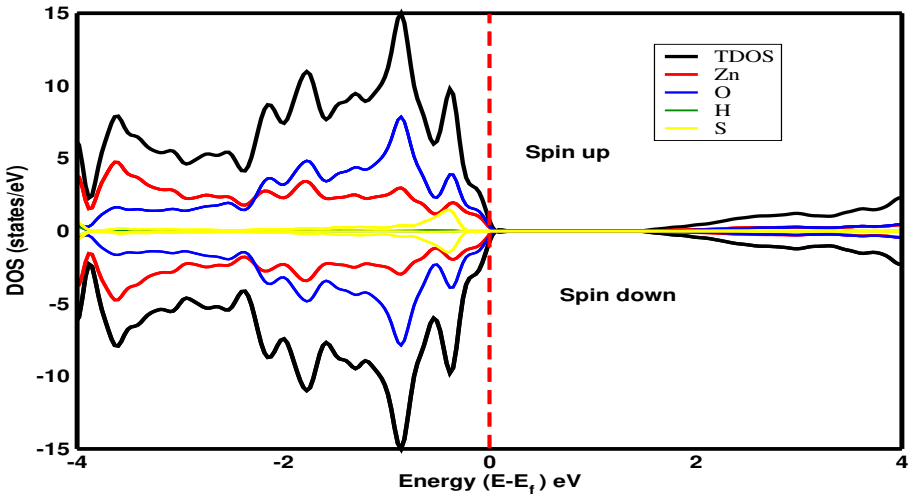

Figure 4.27: Spin polarised DOS of H_2S adsorbed ZnO monolayer, which is obtained by PBE functional.

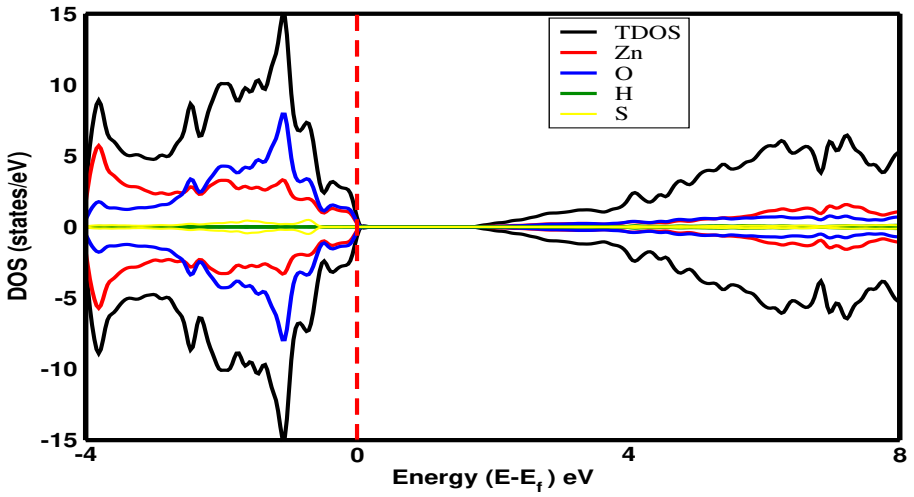

Figure 4.28: Spin polarised DOS of H_2S adsorbed ZnO monolayer, which is obtained by SCAN functional.

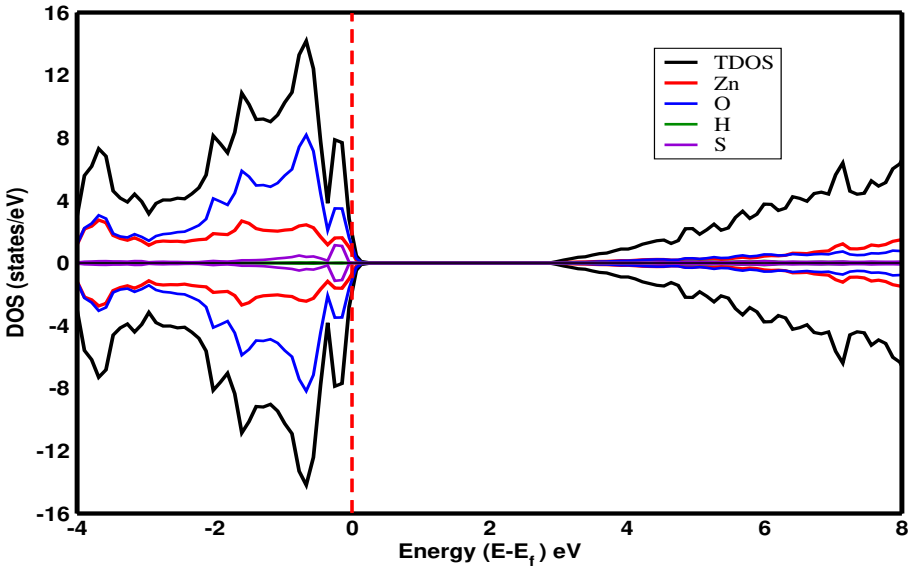

Figure 4.29: Spin polarised DOS of H_2S adsorbed ZnO monolayer, which is obtained by DFT+U functional.

4.3.4 Electronic properties of HCN Adsorbed ZnO monolayer

Figure 4.30 implies the band structure of HCN absorbed ZnO, obtained by using PBE, SCAN, and DFT+U functional. The Fermi level, which is set to 0 eV, is shown by the horizontal blue dashed line. However, the vertical dashed line suggests the high symmetric K-points. The band gap widened in comparison to the pristine monolayer when HCN was adsorbed there. The calculated band energy is 1.50 eV, 1.75 eV, and 3.02 eV for PBE, SCAN, and DFT+U respectively.

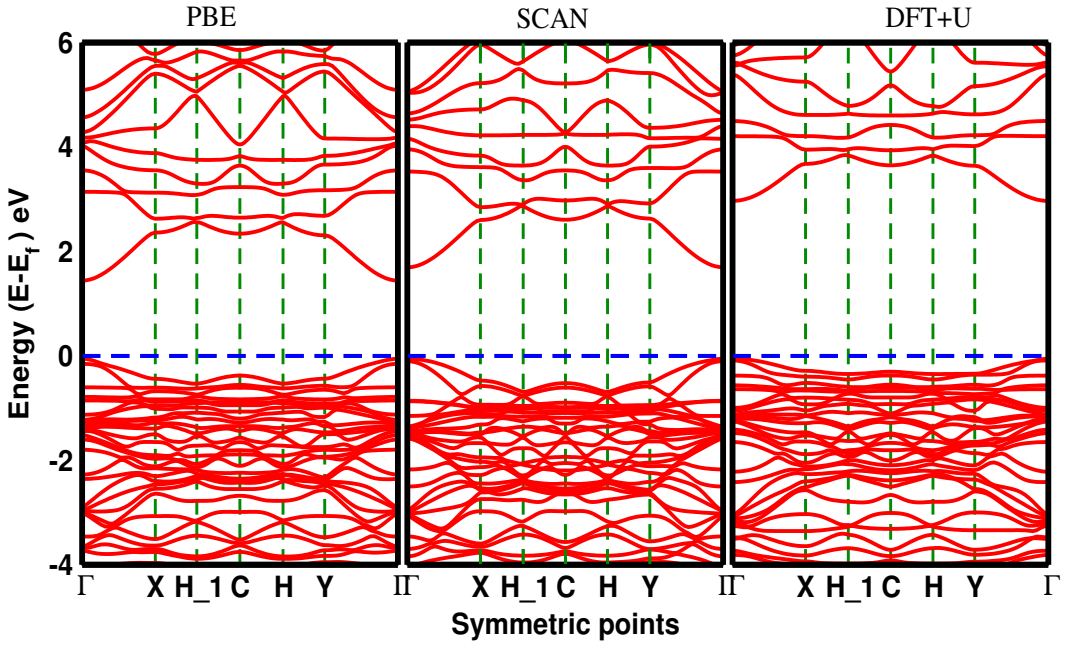

Figure 4.30: Band structure of *HCN* adsorbed *ZnO* monolayer, which is obtained by using PBE, SCAN, and DFT+U functional.

Figures 4.31, 4.32, 4.33 illustrate the band and DOS of the HCN adsorbed ZnO monolayer using PBE, SCAN, and DFT+U functional. The horizontal blue dashed line stands for the Fermi level, set to 0 eV. Thus calculated Fermi energies for PBE, SCAN, and DFT+U are -1.54 eV, -1.42 eV, and -2.12 eV, respectively. The Band and DOS thus calculated closely match with each other. The highest density of states is found near -1 eV, which is around 28 states/eV in PBE functional. Similarly, the highest density of the state is extracted near - 1 eV in SCAN, which is 37 states/eV. Moreover, the highest density of states in DFT+U is found near -1 eV, which is almost 17 states/eV.

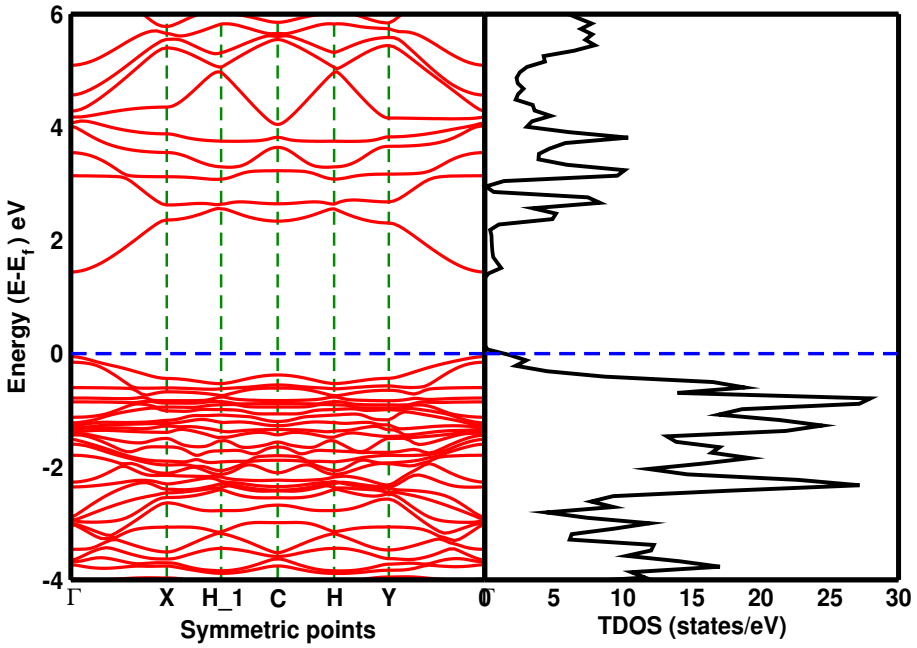

Figure 4.31: Band and DOS structure of *HCN* adsorbed *ZnO*, which is obtained by PBE functional.

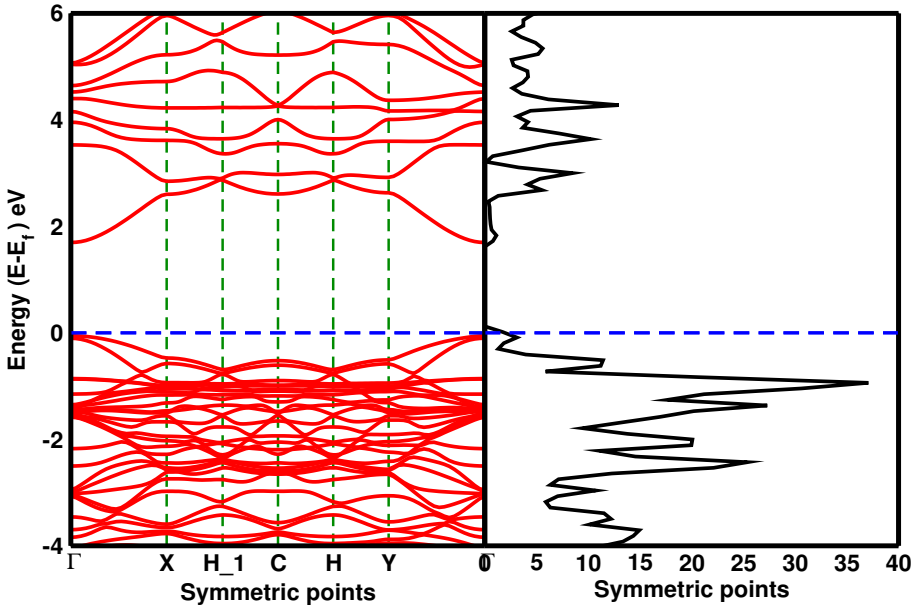

Figure 4.32: Band and DOS structure of *HCN* adsorbed *ZnO*, which is obtained by SCAN functional.

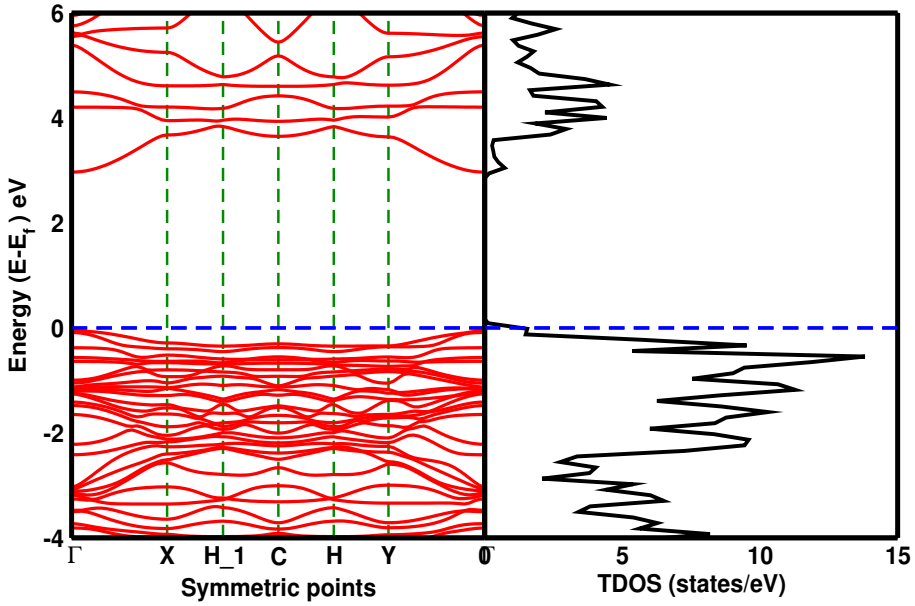

Figure 4.33: Band and DOS structure of *HCN* adsorbed *ZnO*, which is obtained by DFT+U functional.

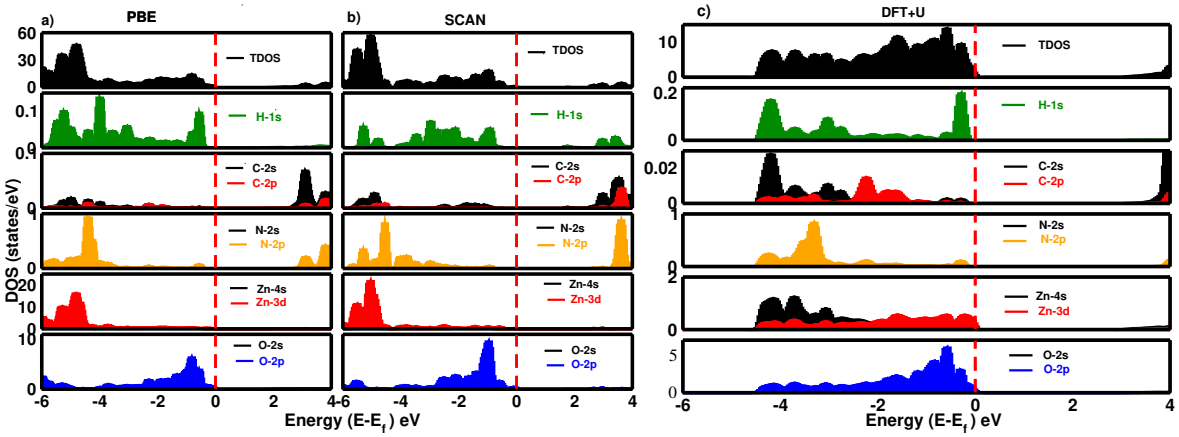

Figure 4.34: PDOS of *HCN* adsorbed *ZnO*, which is obtained by employing different functional: (a) PBE, (b) SCAN, and (c) DFT+U

The projection of the valance orbitals of each atom in the DOS using various functionals is shown in figure 4.34 where the vertical red dash line represents the fermi level, which is set to 0 eV. The orbital contributions of the Zn-3d, Zn-4s, O-2s, O-2p, H-1s, C-2s, C-2p, N-2s,and N-2p are shown in the respective figures. The highest peak in the TDOS is obtained between -4 eV and -5 eV in the valance band, which is due to H-1s, Zn-3d, N-2p, and O-2p orbitals in PBE and SCAN functionals. Similarly, peaks found near the fermi level are due to the H-1s and O-2p orbitals. However, DFT+U functional peaks are found near -4eV due to H-1s, C-2s, and Zn-4s. Similarly, the peak near the

Fermi level is due to the contribution of H-1s, Zn-3d, and O-2p orbitals.

4.3.4.1 Magnetic properties

Three separate exchange-correlation functionals are used to gain information about the spin-polarized density of the state, which is shown in figure 4.35, 4.36, and 4.37. The Fermi level, which is set to zero, is indicated by the vertical red dashed line. We discovered the symmetry between the spin-up and spin-down characteristics of DOS. Additionally, we discovered that the magnetic moment for each of them is zero. We can therefore claim that the system under examination is non-magnetic.

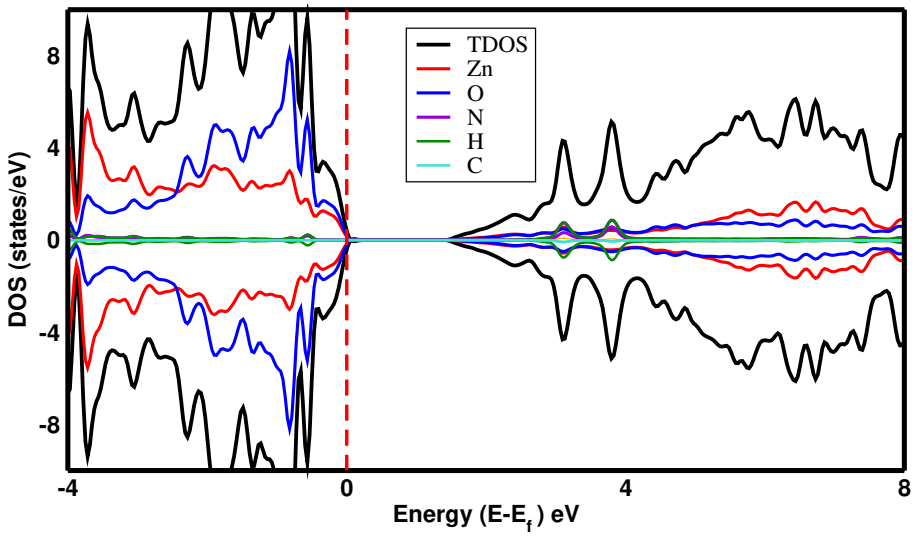

Figure 4.35: Spin polarised DOS of HCN adsorbed ZnO monolayer, which is obtained by using PBE functional.

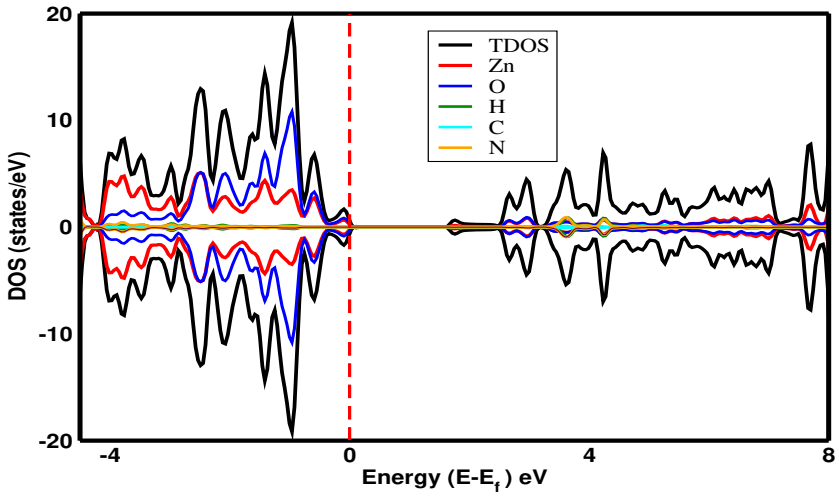

Figure 4.36: Spin polarised DOS of HCN adsorbed ZnO monolayer, which is obtained by using SCAN functional.

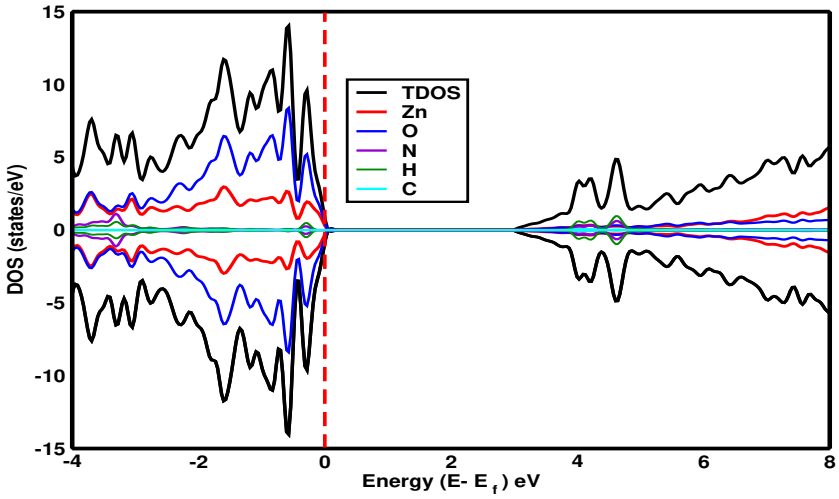

Figure 4.37: Spin polarised DOS of HCN adsorbed ZnO monolayer, which is obtained by using DFT+U functional.

4.3.5 Electronic properties of H_2S adsorbed Al-doped ZnO

Figure 4.38 depicts the band structure of H_2S adsorbed Al-doped ZnO monolayer using various exchange-correlational functional. The blue horizontal dash line in the figure implies the Fermi level, which is adjusted to 0 eV. Similarly, the vertical dot lines represent the symmetric points. The computed band energy for PBE, SCAN, and DFT+U are 0.71 eV, 0.80 eV, and 1.06 eV respectively. It is clearly seen that the energy state shifted toward the valance band, which implies that the system's conductivity increased.

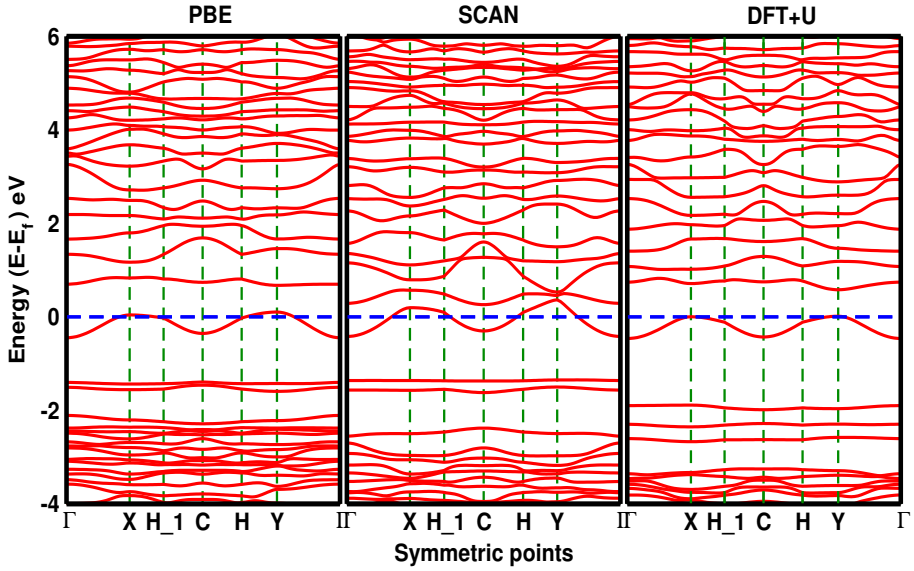

Figure 4.38: Band structure of H_2Sadsorbed Al-doped ZnO, which is obtained by employing different exchange-correlation functionals

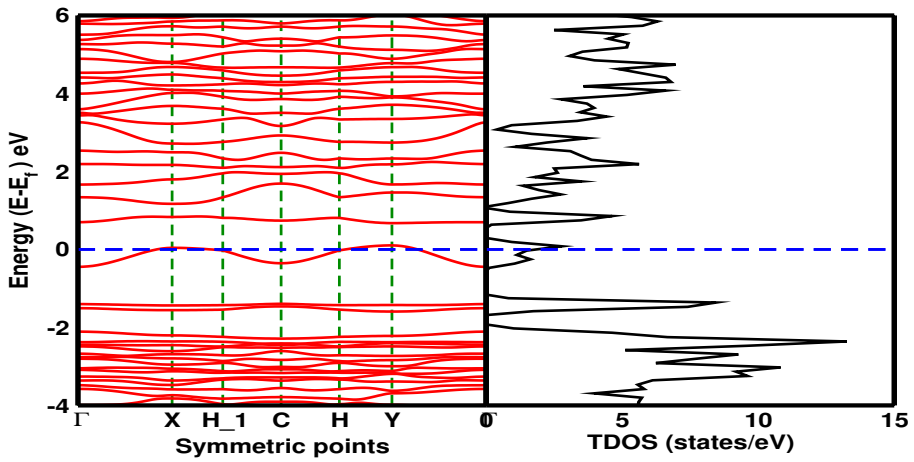

Figure 4.39: Band and DOS structure of H_2S adsorbed Al-doped ZnO monolayer by using PBE functional

Figure 4.39 implies the band and DOS of H_2S adsorbed Al-doped ZnO, which is obtained by employing PBE exchange-correlation functional. Using PBE, we explore the highest density of states at the energy level -1 eV, which is almost 14 states/eV. However, in figure 4.40 and 4.41, the highest density of states is obtained at the energy levels 5 eV, and -3 eV when SCAN and DFT+U are employed. The highest density of states is almost 8 states/eV for both of the functional.

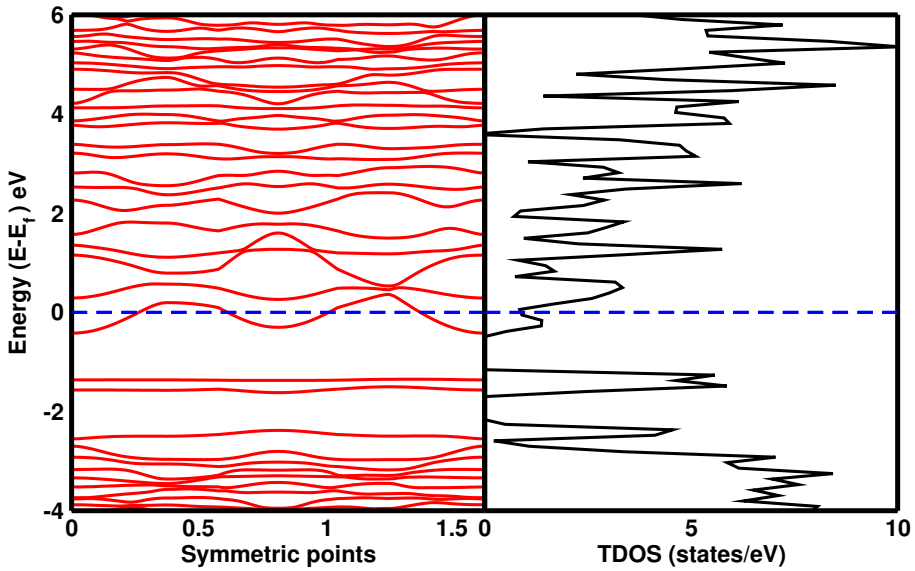

Figure 4.40: Band and DOS structure of H_2S adsorbed Al-doped ZnO monolayer by using SCAN functional

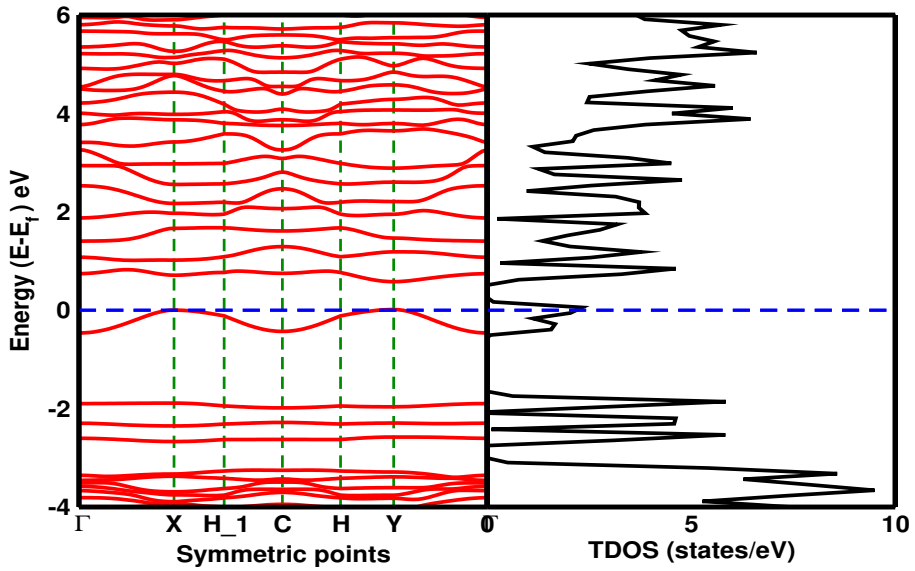

Figure 4.41: Band and DOS structure of H_2S adsorbed Al-doped ZnO monolayer by using DFT+U functional

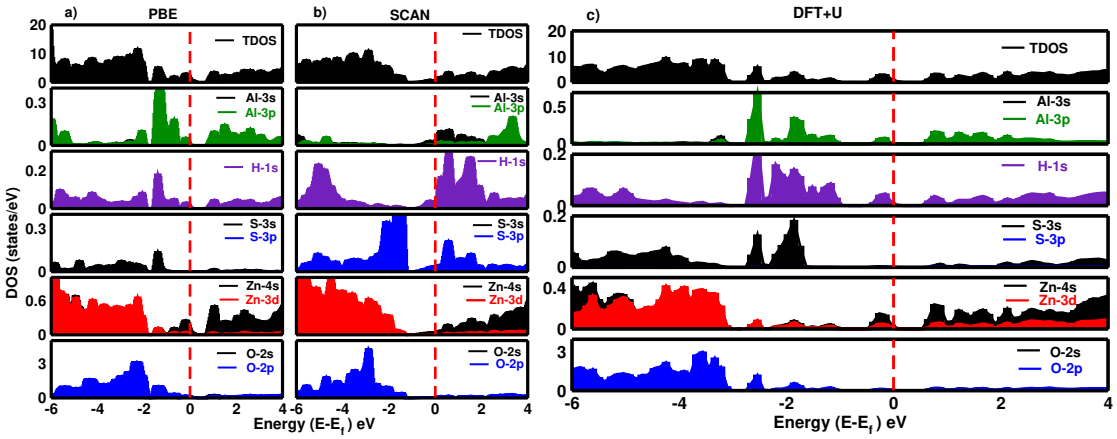

Figure 4.42: PDOS of H_2S adsorbed $Al-$doped ZnO, which is discovered by employing different functional: (a) PBE, (b) SCAN, and (c) DFT+U

Figure 4.42 displays the projection of the valance orbitals of each atom in the DOS using a variety of functionals. The Fermi level, which is set to 0 eV, is represented by the vertical red dashed line. The corresponding figures display the orbital contributions of the Zn-3d, Zn-4s, O-2s, O-2p, Al- 3s, Al-3p, H-1s, S-3s, and S-3p. The peak that was found close to -6 eV is caused by Zn-3d and H-1s, where Al-3p and O-2p made a small but significant contribution to the PBE and SCAN functionals. Similar to this, Al-3p, H-1s, O-2p as well as H-1s, and O-2p respectively have contributed to the peaks near -4 eV and -2 eV. Additionally, peaks are visible close to the Fermi level, which was caused by the orbitals Al-3p, H-1s, and Zn-4s in PBE functional and Al-3s, H-1s, and S-3p by SCAN functionals. Similarly, peaks are seen in the conduction band mainly due to AL-3p, H-1s, S-3p, and Zn-4s orbitals in PBE, and SCAN functionals. When DFT+U functional is employed then peaks are found out in both valance and conduction bands. Peaks between -2 and -4 eV are mainly due to the contribution of H-1s, S-3s, Zn-4s, Zn-3d, and O-2p. Similarly, peaks near about -2 eV are due to Al-3p, H-1s, and S-3p orbitals. Peaks in the conduction band were discovered, which were mainly contributed by Al-3p, H-1s, and Zn-4s orbitals.

4.3.5.1 Magnetic properties

Figure 4.43 elucidates the spin-polarized density of states, which is discovered by employing the PBE exchange-correlation functional. The vertical red dash line represents the Fermi level, which is set to zero. We discovered asymmetry between spin up and

spin down near the Fermi level. Moreover, while calculating the magnetic moment we obtained the magnetic moment of $0.67\mu_B$. Hence, we can ensure the system under study exhibits the magnetic properties. Similarly, the magnetic moment for DFT+U (4.45) is obtained $0.96\mu_B$.

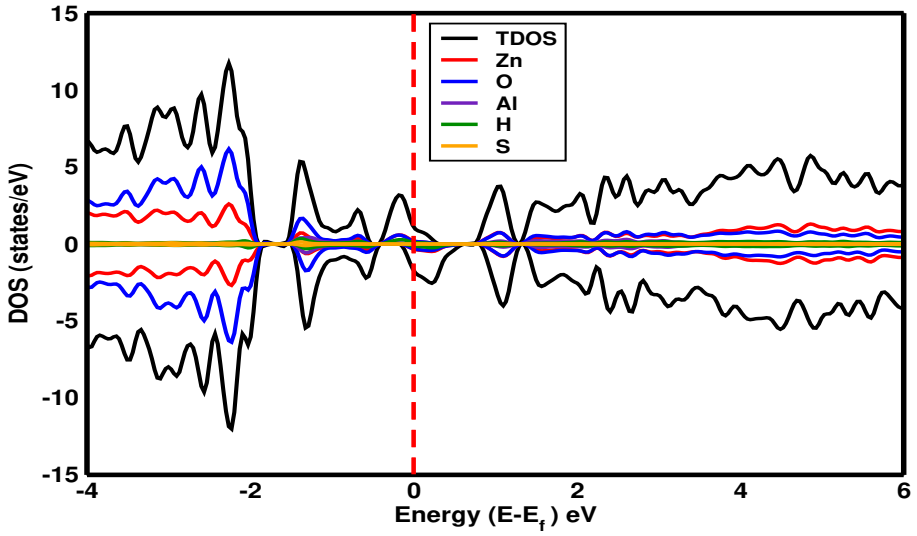

Figure 4.43: Spin up and spin down of H_2S adsorbed $Al-ZnO$, which is obtained by PBE functional.

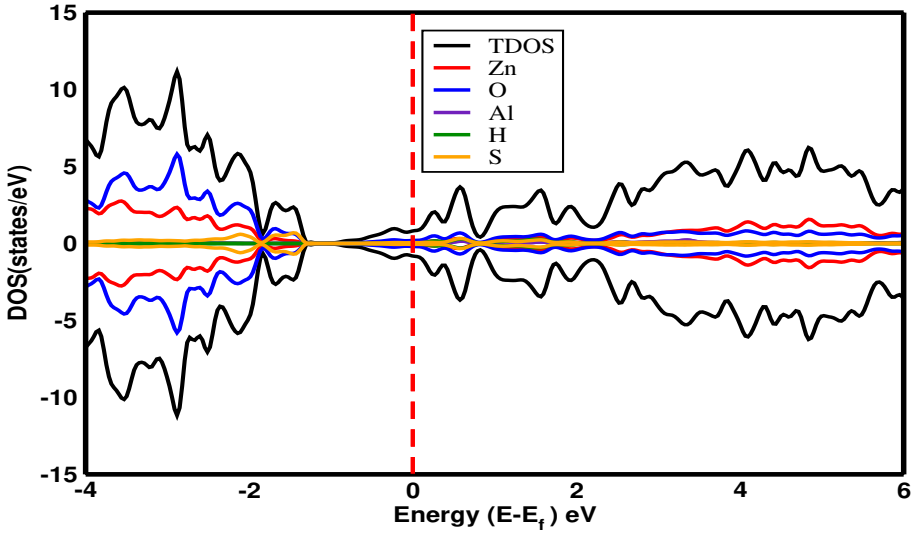

Figure 4.44: Spin up and spin down of H_2S adsorbed $Al-ZnO$, which is obtained by SCAN functional.

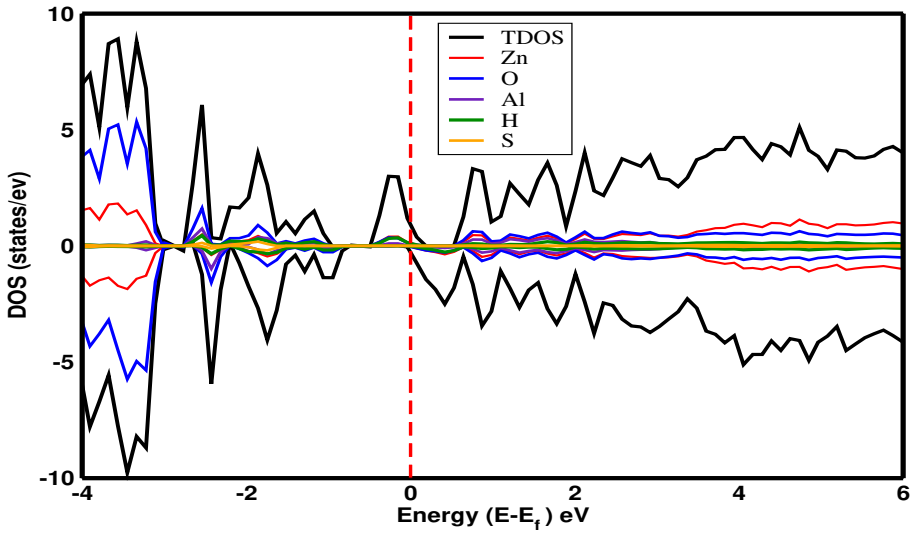

Figure 4.45: Spin up and spin down of H_2S adsorbed $Al-ZnO$, which is obtained by DFT+U functional.

4.3.6 Electronic properties of HCN adsorbed Al-doped ZnO

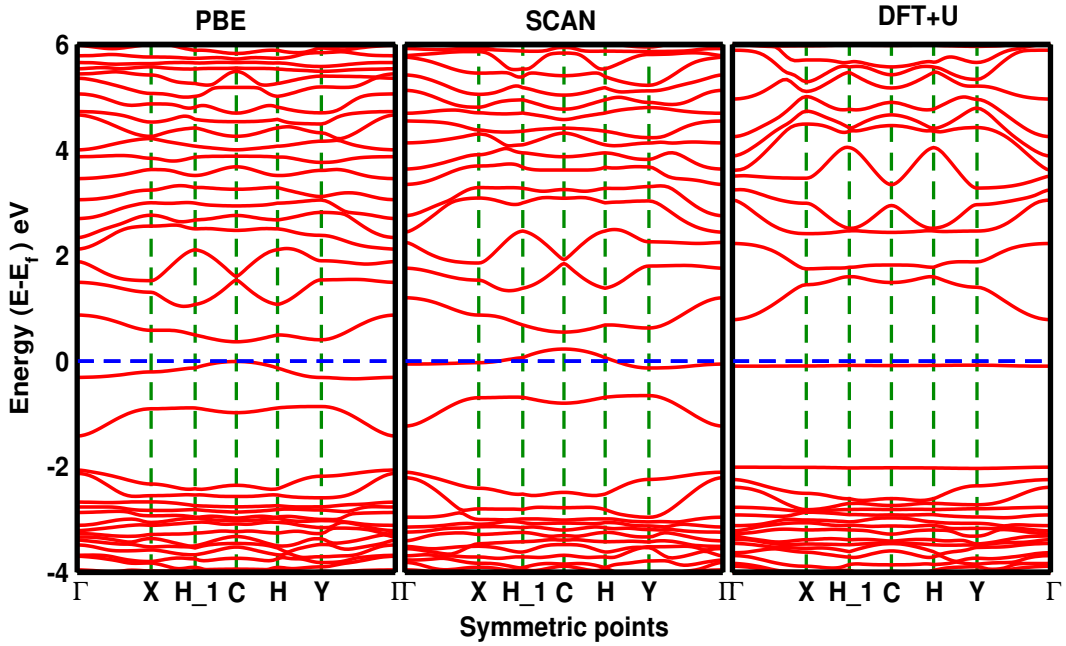

Figure 4.46: Band structure of HCN adsorbed $Al-ZnO$ monolayer, which is obtained by using various functional.

Figure 4.46 shows the band structure of HCN adsorbed $Al-ZnO$, which is discovered by employing the various exchange- correlational functional. The horizontal blue dash line represents the Fermi level which is set to 0 eV. The computed band gap is 0.29 eV,

0.27 eV, and 1.15 eV for HCN using PBE, SCAN, and DFT+U functionals respectively. When Aluminium is doped in the HCN adsorbed ZnO, the fermi level shifts downwards from conduction. As the band shifts downward, the band gap gets reduced significantly as compared to the ZnO monolayer and HCN adsorbed ZnO. The bands thus obtained do not lie on the same K-points which shows that the band is an indirect band gap.

Figure 4.47, 4.48, and 4.49 shows the band and DOS plot of HCN adsorbed Al-doped ZnO, which is found out by employing PBE, SCAN, and DFT+U functionals. In all three functionals, the highest density of states was obtained and found near -3eV in the valance band. Similarly, the highest density of states is found in the valance band from 2 eV to 6 eV in all the functionals. The highest density thus obtained are 13 states/eV, 23 states/eV, and 12 states/eV for PBE, SCAN, and DFT+U functionals respectively. Similarly, the density of the states is discovered near the Fermi level and valance band. The highest density of states is 12 states/eV, 20 states/eV, and 7 states/eV for PBE, SCAN, and DFT+U functional respectively.

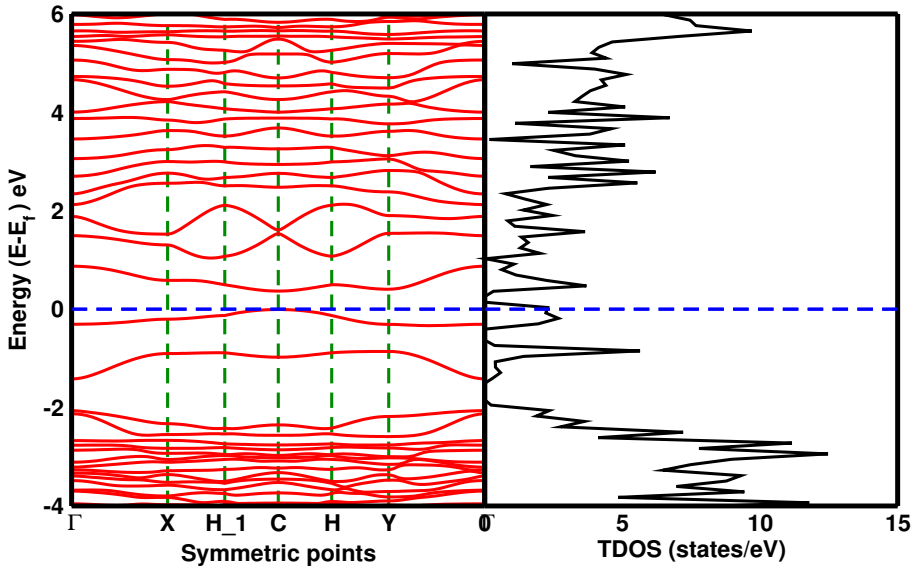

Figure 4.47: Band and DOS of HCN adsorbed $Al-ZnO$, which is obtained by employing PBE exchange-correlation functional

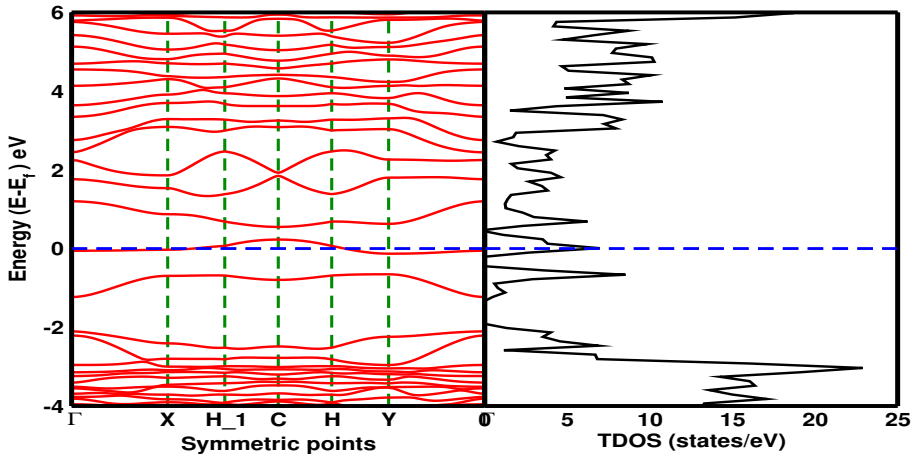

Figure 4.48: Band and DOS of HCN adsorbed $Al - ZnO$, which is obtained by employing SCAN exchange-correlation functional

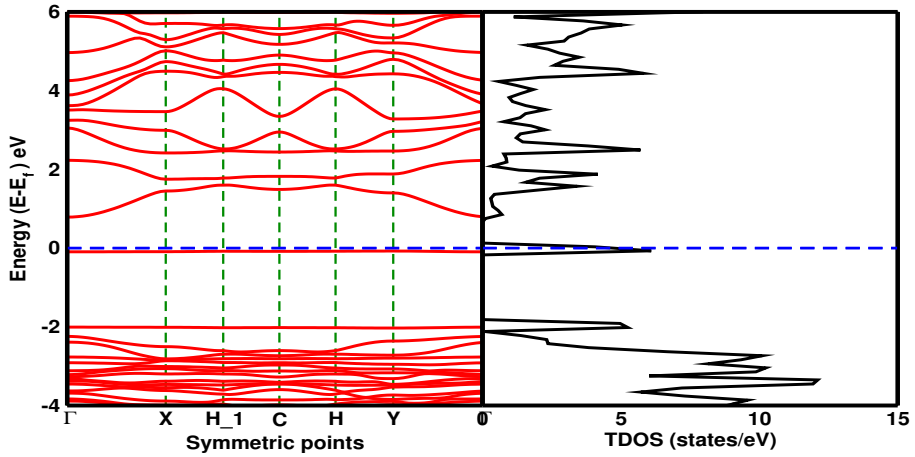

Figure 4.49: Band and DOS of HCN adsorbed $Al - ZnO$, which is obtained by employing DFT+U exchange-correlation functional

Figure 4.50 displays the projection of the valance orbitals of each atom in the DOS using a variety of functionals. The Fermi level, which is set to 0 eV, is represented by the vertical red dashed line. The corresponding figures display the orbital contributions of the Zn-3d, Zn-4s, O-2s, O-2p, Al- 3s, Al-3p, H-1s, C-2s, C-2p, N-2s, and N-2p. The peak that was found close to -6 eV is caused by Zn-3d whereas N-2p. Al-3p, C-2p, and O-2p all made a small but significant contribution to this in the PBE and SCAN functionals. Similar to this, Al-3p, N-2p, and O-2p as well as H-1s, C-2s, and O-2p respectively contribute to the peaks near -4 eV and -2 eV. Additionally, tiny peaks were visible close to the Fermi level, caused by the elements Zn-4s and Al-3p. On the other side, Al-3p, C-2p, and N-2p are responsible for the conduction band's peaks between 2

eV and 4 eV. Figures 4.50 a, and b show that Zn-3d has a very minor contribution. Al-3p, H-1s, C-2p, and N-2p caused a peak in the Fermi level when the DFT+U functional was applied. The peak in the valance band, which is close to -6 eV, is also caused by Al-3p and Zn-4s, with just a minor contribution from C-2p, N-2p, Zn-3d, and O-2p. Furthermore, the increased contribution of Zn-3d, and O-2p results in peaks between -2 eV and -4 eV. Al-3p, Al-3s, C-2p, and N-2p peaks were also seen in the conduction band between 2 eV and 4 eV.

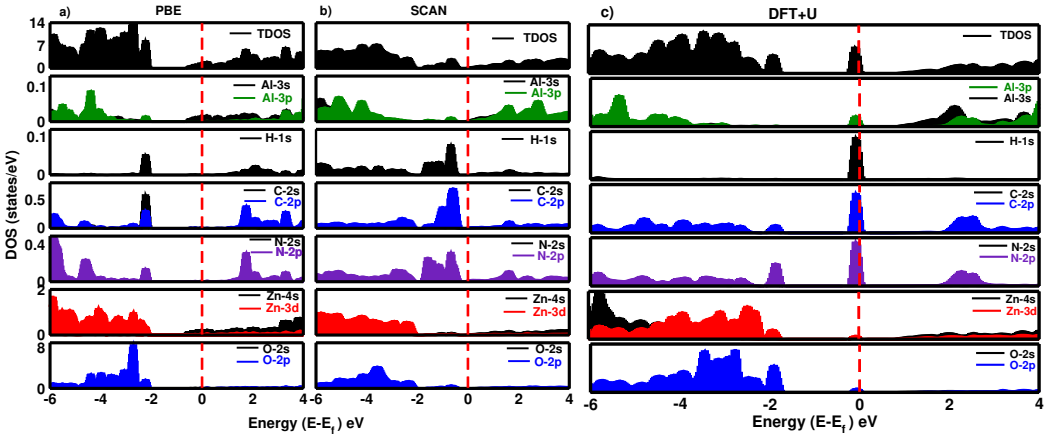

Figure 4.50: PDOS of HCN adsorbed $Al-$ doped ZnO, which is explored by various functional:(a) PBE, (b) SCAN and (d) DFT+U

4.3.6.1 Magnetic properties

Figure 4.51, 4.52, and 4.53 elucidate the spin up and spin down DOS of HCN adsorbed Al-doped ZnO, which is obtained by employing PBE, SCAN and DFT+U exchange-correlational functional. The vertical red dot line represents the Fermi level, set to 0 eV. For PBE functional, we didn't find asymmetry and we can say that the magnetic moment obtained during calculation is zero. However, it is clearly observed that the asymmetry is seen near the Fermi level while employing SCAN and DFT+U, which implies that our system under study might be magnetic. Furthermore, we obtained the magnetic moment of $0.60\mu_B$, and $1.0\mu_B$ for SCAN and DFT+U respectively. So, we can clearly say that the system under investigation is magnetic.

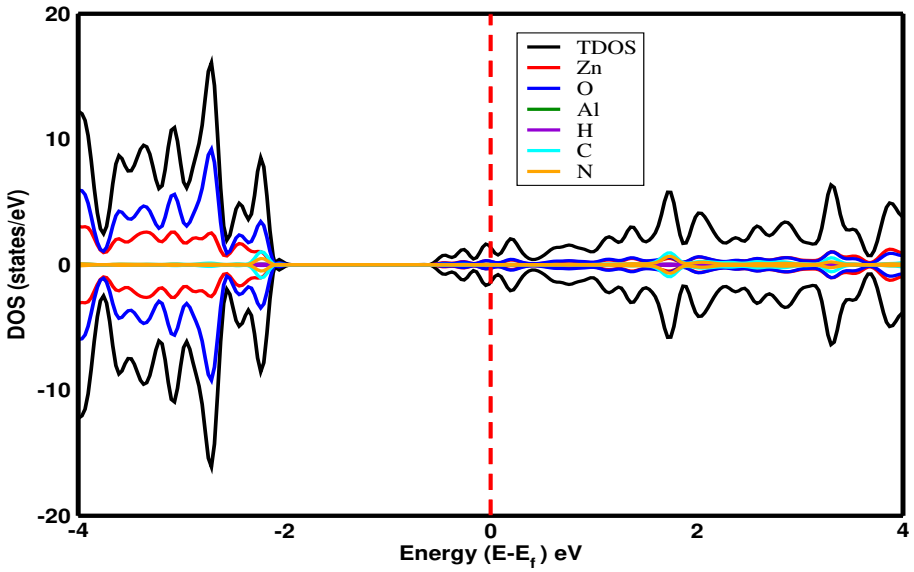

Figure 4.51: Spin up and spin down DOS of HCN adsorbed Al-doped ZnO, which is discovered by employing the PBE functional

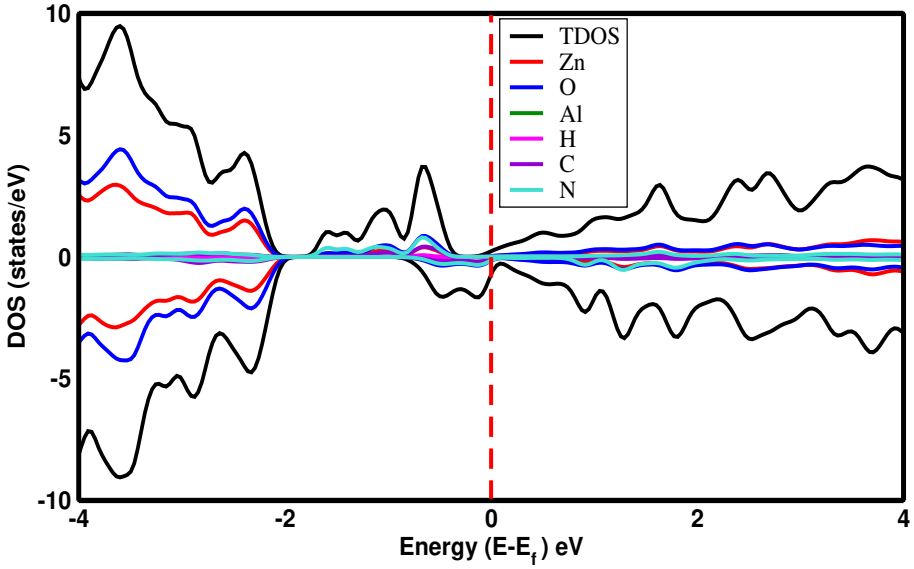

Figure 4.52: Spin up and spin down DOS of HCN adsorbed Al-doped ZnO, which is discovered by employing the SCAN functional

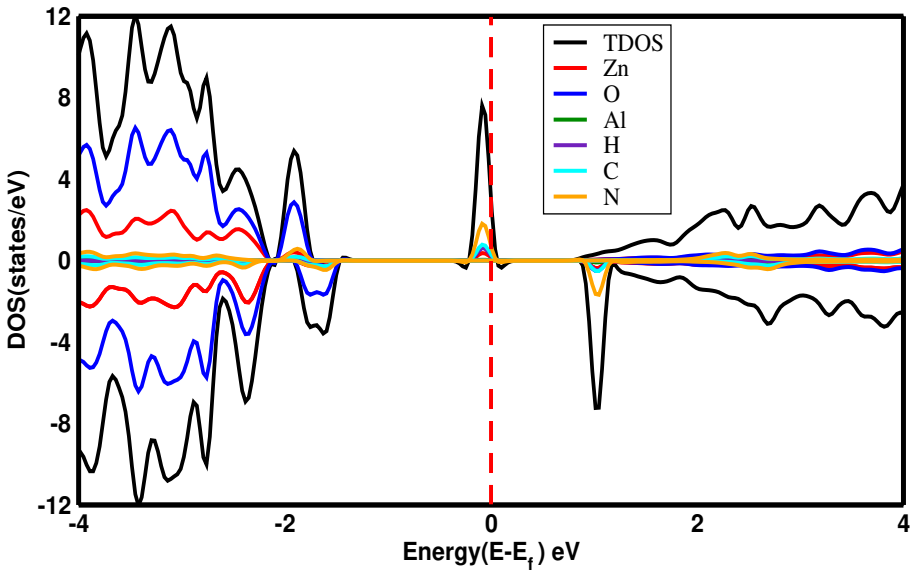

Figure 4.53: Spin up and spin down DOS of HCN adsorbed $Al-$doped ZnO, which is discovered by employing the DFT+U functional

Chapter 5

Conclusions and Future Work

5.1 Conclusions

In this work, we studied the structural, electronic, and magnetic properties of H_2S and HCN adsorbed ZnO and $Al-ZnO$ by employing PBE, SCAN, and DFT+U functionals under Density Functional Theory using VASP codes. We obtained the Band gap of 1.17 eV, 0.96 eV, and 2.61 eV for the ZnO monolayer, 0.07 eV, 0.06 eV, and 0.05eV for Al-doped ZnO, 1.50 eV, 1.77 eV, 2.91 eV for H_2S adsorbed ZnO, 1.50 eV, 1.75 eV, and 3.02 eV for HCN adsorbed ZnO, 0.28eV, 0.26 eV, and 0.024 eV for H_2S adsorbed Al-doped ZnO and 0.21 eV, 0.28eV, and 0.65 eV for HCN adsorbed Al-doped ZnO while using PBE, SCAN and DFT+U functionals respectively. ZnO monolayer, Al-doped ZnO, H_2S, and HCN adsorbed ZnO are found non-magnetic, whereas H_2S, and HCN adsorbed Al-doped ZnO shows magnetic properties. Thus obtained magnetic moments are 0.60 μ_B, 0.96 μ_B, and 1 μ_B for HCN adsorbed Al-doped ZnO and 0.30 μ_B,0.67 μ_B, and 0.96 μ_B for H_2S adsorbed Al-doped ZnO which is obtained on employing PBE, SCAN and DFT+U functionals respectively. Moreover, the lattice parameters increase with the increment in the concentration of the foreign elements and thus the computed structural properties are almost similar to the previous work.

5.2 Future Work

By applying PBE, SCAN, and DFT+U functionals using VASP codes, we studied the structural, electrical, and magnetic properties of H_2S and HCN adsorbed ZnO and Al-doped ZnO. This is just a step in studying the aforementioned properties of the system, while there are optical, mechanical, and other various properties yet to be explored, which we want to carry on through our future research activities, where higher functions like HSEO6, HSE03, and so on will be used to investigate this system.

The study of such types of properties of various systems holds great importance in the sector of digital electronics. Improvement of transistors, diodes, and other applications is facilitated by such studies. So, our future research will be imperative in contributing to technological innovations which will help in uplifting technological revolutions in Nepal too. In future endeavors, we are looking forward to studying the system that replaces the oxygen atom by doping the system with an Aluminum atom and other doping agents, where we can even raise the doping concentration in order to research the system's different characteristics. And, based on the observations made through these experiments, I plan to practically utilize them in technological applications. The findings will surely be beneficial in determining the national economy through technological prosperity as it will have a multitude of positive effects in the various sectors. Besides, our future study will focus on the application of similarly working software like Quantum Espresso, CASTEP, and so on, in order to study different attributes of ZnO as well as other compounds, and the results thus obtained can be compared not only with the standard result but also among each other, which will provide an upper hand to select the best methods for other future studies.

References

[1] A. Singh and H. Vishwakarma, Appl. Phys **6**, 28 (2014).

[2] G. Kresse and J. Furthmüller, Phys. Rev. B **47**, 558 (1993).

[3] M. Ashton, J. Paul, S. B. Sinnott, and R. G. Hennig, Phys. Rev. Lett. **118**, 106101 (2017).

[4] M. Zeng, Y. Xiao, J. Liu, K. Yang, and L. Fu, Chem. Rev. **118**, 6236 (2018).

[5] I. Bouziani, M. Kibbou, Z. Haman, Y. Benhouria, I. Essaoudi, A. Ainane, and R. Ahuja, Phys. Scripta **95**, 015804 (2019).

[6] K. Harun, N. A. Salleh, B. Deghfel, M. K. Yaakob, and A. A. Mohamad, Res. in Phys. **16**, 102829 (2020).

[7] R. R. Reeber, J. Appl. Phys **41**, 5063 (1970).

[8] X. Ma, Y. Wu, Y. Lv, and Y. Zhu, J. Phys. Chem. C **117**, 26029 (2013).

[9] X. Jia, Q. Hou, Z. Xu, and L. Qu, J. Magn. and Magn. Mater. **465**, 128 (2018).

[10] Q. Wang, Q. Sun, P. Jena, Z. Hu, R. Note, and Y. Kawazoe, Appl. Phys. Lett. **91** (2007).

[11] A. Zunger and O. I. Malyi, Chem. Rev. **121**, 3031 (2021).

[12] Z. Jin, T. Fukumura, M. Kawasaki, K. Ando, H. Saito, T. Sekiguchi, Y. Yoo, M. Murakami, Y. Matsumoto, T. Hasegawa, *et al.*, Appl. Phys. Lett. **78**, 3824 (2001).

[13] K. Ellmer and A. Bikowski, J. Phys. D: Appl. Phys. **49**, 413002 (2016).

[14] J. Bartl and M. Baranek, Meas. sci Rev. **4**, 31 (2004).

[15] A. Dabrowski, Adv. Sci. **93**, 135 (2001).

[16] P. S. Kolhe, A. B. Shinde, S. Kulkarni, N. Maiti, P. M. Koinkar, and K. M. Sonawane, J of All. and Comp. **748**, 6 (2018).

[17] R. Reiffenstein, W. C. Hulbert, and S. H. Roth, Ann. Rev. of pharm. and Toxi. **32**, 109 (1992).

[18] M. Yaakob, N. Hussin, M. Taib, T. Kudin, O. Hassan, A. Ali, and M. Yahya, Int. Ferro. **155**, 15 (2014).

[19] C. Tan, D. Sun, X. Tian, and Y. Huang, Mat. **9**, 877 (2016).

[20] H.-C. Wu, Y.-C. Peng, and C.-C. Chen, Opt. Mater. **35**, 509 (2013).

[21] M. Wu, D. Sun, C. Tan, X. Tian, and Y. Huang, J. Mater. **10**, 359 (2017).

[22] D. R. Lawati, H. K. Neupane, D. K. Chaudhary, P. Shrestha, R. P. Adhikari, L. P. Joshi, and R. Parajuli, J Phys. and Chem. Solids **186C**, 111547 (2023).

[23] B. Qiao, P. Zhao, Z. Wang, J. Xiong, Y. Hu, S. Yang, H. Xu, and H. Gu, Comp. and Theo. Chem. **1180**, 112829 (2020).

[24] D. Ma, Q. Wang, T. Li, Z. Tang, G. Yang, C. He, and Z. Lu, J Mater. Chem. C **3**, 9964 (2015).

[25] S. Rezaie, Z. G. Bafghi, and N. Manavizadeh, Intern. J of H. Ene. **45**, 14174 (2020).

[26] Z. Pan, J. Wang, Q. Si, T. Shi, and S. Ma, Comp. and Theo. Chem. **1204**, 113429 (2021).

[27] M. Born and R. Oppenheimer, in *Quantum Chemistry: Classic Scientific Papers* (World Scientific, 2000) pp. 1–24.

[28] J. Han, L. Zhang, and E. Weinan, J. Comp. Phys **399**, 108929 (2019).

[29] J. C. Slater, Phy. Rev. **81**, 385 (1951).

[30] W. Koch, "Holthausen, mc: A chemist's guide to density functional theory," (2001).

[31] E. Engel, *Density Functional Theory* (Springer, 2011).

[32] M. Ernzerhof and G. E. Scuseria, Theo. Chem. **103**, 259 (2000).

[33] L. J. Sham and W. Kohn, Phys. Rev. **145**, 561 (1966).

[34] W. Kohn and L. J. Sham, Phys. Rev. **140**, A1133 (1965).

[35] R. Chimata, "Optical properties of materials calculated from first principles theory," (2010).

[36] J. Sun, A. Ruzsinszky, and J. P. Perdew, Phys. Rev. Lett. **115**, 036402 (2015).

[37] K. Momma and F. Izumi, J of Appl. Cryst. **41**, 653 (2008).

[38] V. Wang, N. Xu, J.-C. Liu, G. Tang, and W.-T. Geng, Com. Phys. Commu. **267**, 108033 (2021).

[39] A. Jain, S. P. Ong, G. Hautier, W. Chen, W. D. Richards, S. Dacek, S. Cholia, D. Gunter, D. Skinner, and G. Ceder, APL Mater. **1** (2013).

[40] L. Honglin, L. Yingbo, L. Jinzhu, and Y. Ke, Phys. Scri. **90**, 025803 (2015).

[41] C. Supatutkul, S. Pramchu, A. Jaroenjittichai, and Y. Laosiritaworn, in *J Phys.*, Vol. 901 (IOP Publishing, 2017) p. 012172.

[42] A. Slassi, S. Naji, A. Benyoussef, M. Hamedoun, and A. El Kenz, J. All. and Comp. **605**, 118 (2014).

Appendix A

Input File Information

A.1 INCAR file for relxation

SYSTEM =	ZnO
ISTART =	0
ICHARGE =	2
	ELECTRONIC OPTIMIZATION
PREC =	ACCURATE
ENCUT =	520 1.3 Times Of EMAX in POTCAR
ISMEAR =	0
SIGMA =	0.05
EDIFF =	1E-07
LREAL =	.FALSE.
	IONIC RELAXATION
EDIFFG =	-1E-02
NSW =	100
ISIF =	3
IBRION =	2

A.2 INCAR For Scf Calculation

SYSTEM =	ZnO
ISTART =	0
ICHARGE =	2
	ELECTRONI OPTIMIZATION
PREC =	ACCURATE
ENCUT =	520
ISMEAR =	0
SIGMA =	0.05
EDIFF =	1E-07
LREAL =	.FALSE.
	IONIC RELAXATION
NSW =	0
IBRION =	-1
NCORE =	2
LWAVE =	.TRUE.
ICHARGE =	.TRUE.

A.3 DOS and BAND CALCULTION

SYSTEM =	ZnO
PREC =	ACCURATE
ISTART =	1
ICHARGE =	11
ENCUT=	520
ISMEAR =	-5
LORBIT =	11
NEDOS =	1000
EDIFF =	1E-07
LREAL =	.FALSE.
NSW=	0
LWAVE=	.FALSE.
LCHARGE =	.TRUE.

A.4 INCAR for different functional

	For PBE Functional
GGA =	PE
	For META-GGA SCAN
METAGGA=	SCAN
LASPH =	.TRUE.
ADDGRID =	.TRUE.
XC=	11
	For DFT+U
LDAU =	.TRUE.
LDAUTYPE =	2
LMAXMIX=	4
LDAUL=	2 1
LDAUU=	10 7
LDAUJ=	0 0